

STRUCTURE-PRESERVING FINITE-ELEMENT APPROXIMATIONS OF THE MAGNETIC EULER-POISSON EQUATIONS

JORDAN HOFFART*, MATTHIAS MAIER*, JOHN N. SHADID†, AND IGNACIO TOMAS‡

Abstract. We develop a structure-preserving numerical discretization for the electrostatic Euler-Poisson equations with a constant magnetic field. The scheme preserves positivity of the density, positivity of the internal energy and a minimum principle of the specific entropy, as well as global properties, such as total energy balance. The scheme uses an operator splitting approach composed of two subsystems: the compressible Euler equations of gas dynamics and a source system. The source system couples the electrostatic potential, momentum, and Lorentz force, thus incorporating electrostatic plasma and cyclotron motions. Because of the high-frequency phenomena it describes, the source system is discretized with an implicit time-stepping scheme. We use a PDE Schur complement approach for the numerical approximation of the solution of the source system. Therefore, it reduces to a single non-symmetric Poisson-like problem that is solved for each time step.

Our focus with the present work is on the efficient solution of problems close to the magnetic-drift limit. Such asymptotic limit is characterized by the co-existence of slowly moving, smooth flows with very high-frequency oscillations, spanning timescales with a difference in excess of $\mathcal{O}(10^{10})$, making their numerical solution quite challenging.

We illustrate the capability of the scheme by computing a diocotron instability and present growth rates that compare favorably with existing analytical results. The model, though a simplified version of the Euler-Maxwell's system, represents a stepping stone toward electromagnetic solvers that are capable of working in the electrostatic and magnetic-drift limits, as well as the hydrodynamic regime.

Key words. Magnetic Euler-Poisson equations, Lorentz force, operator splitting, invariant domain preservation, PDE Schur complement, magnetic drift limit, discrete energy balance.

AMS subject classifications. 65M22, 35L65, 35Q31

1. Introduction. Understanding the mathematical behavior of PDE models describing electric charge transport and magnetic drift-limits is a topic of continuous and active research. In this paper, the main regime of interest is the so-called $E \times B$ -drift limit, also called guiding center drift limit, or simply *magnetic-drift limit*. The mathematical understanding of kinetic models and corresponding numerical schemes in the context of the magnetic-drift limit, and generally speaking the modeling of *strongly magnetized plasmas*, is a topic that has received significant attention in the last two decades [3, 5, 15, 20, 21, 22, 24, 32, 33, 41]. However, the amount of published work related to the robust numerical approximation of the magnetic-drift limit using fluid models is rather scarce; we refer to [6, 14] as notable exceptions.

For both, kinetic and fluid models, the problem is hard enough such that a few strong assumptions are usually made in order to make some analytical or computational progress. For instance, standard assumptions are that the B -field is perfectly perpendicular to the velocity field. Similarly, it is very common to assume that the E -field and/or the magnetic field B are *given*, rather than computed self-consistently from the evolution equations. In this paper we assume that the magnetic field B is

*Department of Mathematics, Texas A&M University, 3368 TAMU, College Station, TX 77843, USA ({jordanhoffart, maier}@tamu.edu)

†Sandia National Laboratories¹, P.O. Box 5800, MS 1320, Albuquerque, NM 87185, USA (jnshadi@sandia.gov); and Department of Mathematics and Statistics, University of New Mexico, MSC01 1115, Albuquerque, NM 87131, United States

‡Department of Mathematics and Statistics, Texas Tech University, 2500 Broadway, Lubbock, TX 79409, USA (igtomas@ttu.edu)

given, but the electric field \mathbf{E} is computed self-consistently from the evolution equations. This allows, in particular, to focus on developing a computationally efficient time integration technique with mathematical guarantees of structure preservation. Some basic questions of practical interest are: What components of the system can be treated using explicit time integration, and what parts require the use of implicit methods? What structural properties need to be preserved?

Our goal with the present publication is to develop a numerical method for the magnetic Euler-Poisson system that is (a) provably *robust*, this is to say, it preserves relevant solution structure on the *fully discrete* level, and (b) allows to solve linear subproblems efficiently without the need to resolve the very fast time scales of electrostatic plasma and cyclotron high frequency oscillations.

The outline of the paper is as follows: Section 2 discusses preliminary aspects on the Euler system, the Euler-Poisson system with a given magnetic field and its time-scales, and the magnetic-drift limit. Section 3 describes the operator splitting approach and the PDE Schur complement (see Section 3.2) technique used to solve the corresponding linear system. Section 4 provides a fully discrete description of the scheme as well as a few theoretical results about the scheme. Section 5 provides validation results as well as computations of the diocotron instability with validation of growth rates. The current work is part of the research program outlined by the authors in [40], as well as in two lab reports [47, 48].

2. Preliminaries. We first introduce the magnetic Euler-Poisson equations and summarize a number of important structural properties of the PDE system. A detailed discussion of the system and key features for the design of numerical methods can be found in [40, 47, 48]. For the sake of completeness we nevertheless summarize a number of key observations in detail that will be important for the design of our numerical method.

2.1. The compressible Euler equations with forces. Let $D \subset \mathbb{R}^d$, $d = 2, 3$, be an open, bounded, simply connected Lipschitz domain with unit outward normal \mathbf{n} . We consider a fluid occupying D with mass density $\rho(\mathbf{x}, t)$, velocity $\mathbf{v}(\mathbf{x}, t) \in \mathbb{R}^d$, momentum (per unit volume) $\mathbf{m} := \rho\mathbf{v}$, pressure $p(\mathbf{x}, t) \in \mathbb{R}$, and total mechanical energy (per unit volume) $\mathcal{E}(\mathbf{x}, t)$. We assume that the fluid motion is given by the compressible Euler equations subject to a force described by $\mathbf{f}(\mathbf{x}, t) \in \mathbb{R}^d$ with units of force per volume. The compressible Euler equations then read,

$$(2.1) \quad \begin{cases} \partial_t \rho + \nabla \cdot \mathbf{m} = 0, \\ \partial_t \mathbf{m} + \nabla \cdot (\rho^{-1} \mathbf{m} \mathbf{m}^\top + \mathbb{I} p) = \mathbf{f}, \\ \partial_t \mathcal{E} + \nabla \cdot (\rho^{-1} \mathbf{m} (\mathcal{E} + p)) = \rho^{-1} \mathbf{m} \cdot \mathbf{f}. \end{cases}$$

Let $\mathbf{u} := [\rho, \mathbf{m}, \mathcal{E}]^T$ denote the combined state vector. We summarize a fundamental observation about the (formal) time evolution of entropies for such a forced system [12, 40, 47, 48]:

LEMMA 2.1. *Let $\Psi(\mathbf{u}) : \mathbb{R}^{d+2} \rightarrow \mathbb{R}$ be a function of the state satisfying the functional dependence $\Psi(\mathbf{u}) := \psi(\rho, e(\mathbf{u}))$, where $e(\mathbf{u}) := \frac{\mathcal{E}}{\rho} - \frac{|\mathbf{m}|^2}{2\rho^2}$ is the specific internal energy. Let $\mathbf{u}(\mathbf{x}, t)$ be a (sufficiently smooth) solution to (2.1). The time evolution of*

$\Psi(\mathbf{u}(\mathbf{x}, t))$ is then formally given by

$$(2.2) \quad \partial_t \Psi(\mathbf{u}) + \nabla_{\mathbf{u}} \Psi(\mathbf{u}) \cdot \begin{bmatrix} \nabla \cdot \mathbf{m} \\ \nabla \cdot (\rho^{-1} \mathbf{m} \mathbf{m}^\top + \mathbb{I} p) \\ \nabla \cdot (\rho^{-1} \mathbf{m} (\mathcal{E} + p)) \end{bmatrix} = 0,$$

where $\nabla_{\mathbf{u}}$ is the gradient with respect to the state. In other words, the time evolution of $\Psi(\mathbf{u}(\mathbf{x}, t))$ does not directly depend on the force field $\mathbf{f}(\mathbf{x}, t)$.

Proof. See [40, Lemma 2.1 and Remark 2.2]. \square

An immediate consequence of the above lemma is the fact that the compressible Euler equations with forces maintain the same entropy and invariant domain structure as the system of equations without forces \mathbf{f} [12, 40]:

COROLLARY 2.2. *Let \mathcal{B} be an invariant domain [29] of the compressible Euler equations that is fully described in terms of density ρ and specific internal energy e of a state \mathbf{u} , such as*

$$\mathcal{B}_* := \left\{ \mathbf{u} \in \mathbb{R}^{d+2} : \rho > 0, e(\mathbf{u}) > 0, s(\rho, e(\mathbf{u})) \geq s_{\min} \right\},$$

where $s(\rho, e(\mathbf{u}))$ denotes the specific entropy. Then, the compressible Euler equations with forces, as described in (2.1) maintains the same invariant domain.

2.2. The Lorentz force. We now assume that the fluid consists of a single electrically charged species, for example, electrons with negative charge. The force \mathbf{f} acting on the fluid is then given by the *Lorentz force* generated by an electric field $\mathbf{E}(\mathbf{x}, t) \in \mathbb{R}^d$ and a magnetic flux density $\mathbf{B}(\mathbf{x}, t) \in \mathbb{R}^{d_*}$:

$$\mathbf{f} := \rho_e \mathbf{E} + \rho_e \mathbf{v} \times \mathbf{B},$$

where $\rho_e(\mathbf{x}, t) := q_e/m_e \rho(\mathbf{x}, t)$ is the electric charge density, and q_e is the *elemental charge* and m_e the *element mass* of the species. For $d = 3$ we simply set $d_* = 3$, and for $d = 2$, we set $d_* = 1$. For $d = 2$, by slight abuse of notation, we set the cross product to $\mathbf{v} \times \mathbf{B} := [v_2, -v_1]^T B$, which corresponds to a *transverse magnetic* configuration, where the fluid motion is confined to the 2D plane spanned by $\hat{\mathbf{e}}_1, \hat{\mathbf{e}}_2$, and the magnetic field has only a component in the $\hat{\mathbf{e}}_3$ -direction.

The time evolution of the electric field $\mathbf{E}(\mathbf{x}, t)$ and the magnetic flux density $\mathbf{B}(\mathbf{x}, t)$ is given by Maxwell's equations where the electric charge density $\rho_e(\mathbf{x}, t)$ and the electric current density $(\rho_e \mathbf{v})(\mathbf{x}, t)$ enter as forcing terms [4]. We make the assumption that the magnetic flux density is constant in time, i.e., $\partial_t \mathbf{B} = \mathbf{0}$, which in turn implies by that $\nabla \times \mathbf{E} = \mathbf{0}$ by virtue of Maxwell's equations. From this and the assumption that D is simply connected, we have that $\mathbf{E} = -\nabla \varphi_e$ for some electric potential $\varphi_e(\mathbf{x}, t)$. Now, we introduce rescaled quantities for the magnetic flux density and the electric potential, and define a coupling constant α [40],

$$\varphi := \frac{q_e}{m_e} \varphi_e, \quad \boldsymbol{\Omega} := \frac{q_e}{m_e} \mathbf{B}, \quad \alpha := \frac{1}{\varepsilon_0} \frac{q_e^2}{m_e^2} > 0.$$

Here, ε_0 is the vacuum permittivity [7]. Then, we can rewrite the Lorentz force acting on the charged fluid and Maxwell's equations describing the evolution of the electric potential [40],

$$\mathbf{f} := -\rho \nabla \varphi + \mathbf{m} \times \boldsymbol{\Omega},$$

$$\partial_t (-\Delta \varphi) = -\alpha \nabla \cdot \mathbf{m}.$$

In summary, we consider the following Euler-Poisson model with magnetic field:

DEFINITION 2.3 (Magnetic Euler-Poisson equations). *Given a rescaled, static, divergence free magnetic flux density $\Omega(\mathbf{x}) \in \mathbb{R}^{d^*}$, and initial data for the state $\mathbf{u}(\mathbf{x}, t) = [\rho, \mathbf{m}, \mathcal{E}]^T$ and the potential $\varphi(\mathbf{x}, t)$ satisfying the compatibility condition*

$$(2.3) \quad -\Delta\varphi = \alpha\rho,$$

find a solution to the evolution equation

$$(2.4) \quad \begin{cases} \partial_t\rho + \nabla \cdot \mathbf{m} = 0, \\ \partial_t\mathbf{m} + \nabla \cdot (\rho^{-1}\mathbf{m}\mathbf{m}^\top + \mathbb{I}p) = -\rho\nabla\varphi + \mathbf{m} \times \Omega, \\ \partial_t\mathcal{E} + \nabla \cdot (\rho^{-1}\mathbf{m}(\mathcal{E} + p)) = -\mathbf{m} \cdot \nabla\varphi, \\ \partial_t(-\Delta\varphi) = -\alpha\nabla \cdot \mathbf{m}, \end{cases}$$

subject to appropriately chosen boundary conditions.

Note that system (2.4) has to be closed with an *equation of state* that determines the pressure $p(\mathbf{u}) = p(\rho, e(\mathbf{u}))$ as a function of the hydrodynamical state \mathbf{u} . In the case of a barotropic closure, where the pressure depends only on the density, the energy equation \mathcal{E} is no longer necessary [18]. The barotropic version of (2.4) is discussed with more detail in Appendix A.

A number of remarks are in order:

Remark 2.4 (Gauß law). The magnetic Euler-Poisson equations (2.4) formally maintain the Gauß law, i. e., if (2.3) is maintained at the initial time, it holds true for all time. More precisely, substituting the first equation of (2.4) into the fourth equation, we observe that

$$\partial_t(-\Delta\varphi - \alpha\rho) = 0.$$

LEMMA 2.5 (Energy balance). *The magnetic Euler-Poisson equations (2.4) admit the following formal energy balance:*

$$(2.5) \quad \begin{aligned} \frac{d}{dt} \int_D \mathcal{E} + \frac{1}{2\alpha} |\nabla\varphi|_{\ell^2}^2 dx \\ + \int_{\partial D} \left\{ \rho^{-1}\mathbf{m}(\mathcal{E} + p) + \varphi(\mathbf{m} - \alpha^{-1}\partial_t\nabla\varphi) \right\} \cdot \mathbf{n} d\sigma_x = 0, \end{aligned}$$

where \mathbf{n} denotes the outwards pointing unit normal on ∂D .

Proof. Test the last equation of (2.4) with $\alpha^{-1}\varphi$ and integrate by parts:

$$\frac{d}{dt} \int_D \frac{1}{2\alpha} |\nabla\varphi|_{\ell^2}^2 dx + \int_{\partial D} \varphi(\mathbf{m} - \alpha^{-1}\partial_t\nabla\varphi) \cdot \mathbf{n} d\sigma_x = \int_D \mathbf{m} \cdot \nabla\varphi dx.$$

Then, integrate the third equation of (2.4) in space, use the Gauß theorem and add the result to the previous equation. \square

The energy balance for the barotropic case is briefly discussed in Appendix A.

2.3. Time scales of the magnetic Euler-Poisson equations. Special care must be taken when discretizing system (2.4) due to the possible presence of highly disparate time scales [40, 47, 48]. With the goal that the time-step size shall only be subject to a *hyperbolic CFL* condition [40] from the Euler subsystem, it is crucial to design the approximation technique such that faster scales can be overstepped safely. System (2.4) contains three time scales.

Hyperbolic time scale T_h . The hydrodynamical subsystem is obtained by removing φ and Ω from (2.4) resulting in the compressible Euler equations without a force. This system is—due to the lack of a viscosity term—*scale free*. Nevertheless, heuristically, we wish to define a hyperbolic time scale T_h as the time scale on which the hyperbolic state \mathbf{u} undergoes significant changes. Concretely, for the fully discrete approximation scheme we can identify such a time scale T_h by identifying it with the maximal admissible time-step size τ_n given by a hyperbolic CFL condition for the n th time step; see Equation (B.8):

$$T_h := \tau_n.$$

With this definition, we will automatically fully resolve the hyperbolic time scale in our numerical computations.

Plasma oscillation time scale $T_p = \omega_p^{-1}$. Another frequency regime present in the (2.4) is the one of plasma oscillations [4, 23]. We can uncover this regime by setting Ω and the hyperbolic flux to zero in (2.4) which yields a limiting equation coupling potential φ and momentum \mathbf{m} [40]:

$$\begin{cases} \partial_t \mathbf{m} = -\rho \nabla \varphi, \\ \partial_t (-\Delta \varphi) = -\alpha \nabla \cdot \mathbf{m}. \end{cases}$$

Now, taking the divergence of the first equation as well as the time derivative of the second, and assuming that the gradient in the density ρ is sufficiently small, we arrive at

$$\Delta(\partial_{tt}\varphi + \omega_p^2 \varphi) = 0, \quad \omega_p := \sqrt{\rho\alpha} = \sqrt{\frac{\rho q_e^2}{\varepsilon_0 m_e^2}}.$$

Consequently, the potential φ (and with it the momentum \mathbf{m} and the density ρ) can exhibit instabilities governed by a simple harmonic oscillator equation. We note that the plasma frequency ω_p can be very large. For most high-energy density applications ω_p typically takes values in the GHz regime; see for instance [4, p. 12] and [23, p. 56].

Cyclotron and diocotron time scales $T_c = \omega_c^{-1}$, $T_d = \omega_d^{-1}$. Another set of critical time scales are related to the presence of the magnetic field \mathbf{B} . Introducing the *cyclotron frequency* $\omega_c := |\Omega|_{\ell^2} = \frac{q_e}{m_e} |\mathbf{B}|_{\ell^2}$ we can identify another subsystem of (2.4) by formally setting the potential φ and the hyperbolic flux to zero, viz.,

$$\partial_t \mathbf{m} = \mathbf{m} \times \Omega.$$

This limiting equation is equivalent to the equation of motion of isolated charged particles subject to a static magnetic field. We note that, in the context of cold low-density plasma physics applications, times scales usually follow the order $T_h^{-1} \ll \omega_p \ll \omega_c$ see [4, 48]. For instance, the cyclotron frequency for isolated electrons in a magnetic field of around 1 Tesla, is approximately 180 GHz [4, 23]. Contrary to the plasma frequency, the cyclotron frequency does not depend on the hydrodynamical state.

We note that, crucially, while the cyclotron frequency ω_c might become very large, the cyclotron motions might not necessarily manifest in the macroscopic dynamics of the fluid. In particular, this is true for the so-called *magnetic-drift* or *guiding center* limit [5, 14, 48]. We derive the drift limit by assuming that inertial terms, temperature, and pressure are negligible, meaning: $\partial_t \mathbf{m} + \operatorname{div}(\rho^{-1} \mathbf{m} \mathbf{m}^\top) \approx \mathbf{0}$ and $\nabla p \approx \mathbf{0}$ in (2.4),

which in turn implies $-\rho\nabla\varphi + \mathbf{m} \times \boldsymbol{\Omega} = \mathbf{0}$. We solve this algebraic side condition by introducing a *drift velocity* [7, Chapter 3] that depends on the prescribed magnetic field and the potential:

$$(2.6) \quad \mathbf{v}_{\text{dr}} := -\frac{\nabla\varphi \times \boldsymbol{\Omega}}{|\boldsymbol{\Omega}|_{\ell^2}^2}.$$

System (2.4) then reduces to a coupled system of density ρ and potential φ :

$$(2.7) \quad \begin{cases} \partial_t \rho + \nabla \cdot (\rho \mathbf{v}_{\text{dr}}) = 0, \\ \partial_t (-\Delta\varphi) = -\alpha \nabla \cdot (\rho \mathbf{v}_{\text{dr}}). \end{cases}$$

Substituting (2.6) into the second equation of (2.7), and performing a dimensional analysis, we can identify a time scale for the dynamics. The resulting time scale is determined by the *diocotron frequency*:

$$T_d = \omega_d^{-1}, \quad \omega_d := \frac{\rho\alpha}{|\boldsymbol{\Omega}|_{\ell^2}} = \frac{\omega_p^2}{\omega_c}.$$

The magnetic drift-limit model (2.7) is, in itself, relatively benign as it is dominated by the slow time-scale T_d and does not contain the fast plasma and cyclotron frequencies. However, designing schemes capable of solving the full magnetic Euler-Poisson system (2.4) that contains the fast scales in a fluid regime where inertial and thermal effects are negligible is non-trivial endeavour [9, 11, 14]. In Section 5 we will present numerical simulations where the time scales $1 \sim T_h^{-1} \sim \omega_d \ll \omega_p \ll \omega_c \sim 10^{12}$ span 12 orders of magnitude.

3. Operator splitting and PDE Schur complement. We now discuss our strategy for approximating solutions to (2.7) that maintain a discrete counterpart of the structural properties outlined in Lemmas 2.1, 2.4, 2.5, and Corollary 2.2. Following the general approach outlined in [40] we first perform an operator split of (2.7) into a hyperbolic operator and a *source update*, and then condense the resulting system on semi-discrete level with a PDE Schur complement [40].

3.1. Operator splitting. The discussion outlined in Section 2 suggests to treat the hydrodynamical subsystem of (2.4) separately from the update induced by the Lorentz force. We thus proceed to approximate solutions to (2.4) by an operator splitting approach. Concretely, we intend to use a second-order *Strang* split (see [46, Ch. 5]), or some form of high-order IMEX split [16, 17].

The *hyperbolic subsystem* is recovered from (2.4) by taking the formal limit $\varepsilon := q_e/m_e \rightarrow 0$:

$$(3.1) \quad \begin{cases} \partial_t \rho + \nabla \cdot \mathbf{m} = 0, \\ \partial_t \mathbf{m} + \nabla \cdot (\rho^{-1} \mathbf{m} \mathbf{m}^\top + \mathbb{I} p) = \mathbf{0}, \\ \partial_t \mathcal{E} + \nabla \cdot (\rho^{-1} \mathbf{m} (\mathcal{E} + p)) = 0, \\ \partial_t \Delta\varphi = 0 \end{cases}$$

Conversely, the *source update subsystem* is recovered from (2.4) by taking the opposite

limit, $\varepsilon := (q_e/m_e)^{-1} \rightarrow 0$ and renormalizing the timescale with $t = \mathcal{O}(\varepsilon)$:

$$(3.2) \quad \begin{cases} \partial_t \rho = 0 \\ \partial_t \mathbf{m} = -\rho \nabla \varphi + \mathbf{m} \times \boldsymbol{\Omega}, \\ \partial_t \mathcal{E} = -\mathbf{m} \cdot \nabla \varphi, \\ \partial_t (-\Delta \varphi) = -\alpha \nabla \cdot \mathbf{m}. \end{cases}$$

With both subsystems at hand Strang splitting takes the following form:

DEFINITION 3.1 (Strang splitting). *Given a state $\mathbf{u}^n = [\rho^n, \mathbf{m}^n, \mathcal{E}^n]$ and potential φ^n at time t_n , compute an update as follows:*

- First, solve the hyperbolic system (3.1) with extended initial state $\{\mathbf{u}^n, \varphi^n\}$ resulting in a time-step size $\tau_n/2$ and an updated state $\{\hat{\mathbf{u}}, \hat{\varphi}\}$.
- Then, solve the source update system (3.2) with initial state $\{\hat{\mathbf{u}}, \hat{\varphi}\}$ and fixed time-step size τ_n resulting in an updated state $\{\check{\mathbf{u}}, \check{\varphi}\}$.
- Finally, solve the hyperbolic system (3.1) a second time with initial state $\{\check{\mathbf{u}}, \check{\varphi}\}$ and fixed time-step size $\tau_n/2$ resulting in a final update $\{\mathbf{u}^{n+1}, \varphi^{n+1}\}$ for time $t_{n+1} = t_n + \tau_n$.

We refer the reader to [12, 26, 40] for a detailed discussion on the use of Strang splitting for related hyperbolic systems.

The methodology developed in this paper can in principle be used with a variety of different numerical discretization techniques for the Euler subsystem (3.1). In the following we simply make the assumption that the choice of discretization and solver for (3.1) maintains conservation, admissibility and a suitable invariant domain on the fully discrete level; see Section 4.2 and Appendix B. We focus in detail on the discretization and structural properties of (3.2).

3.2. A PDE Schur complement. We now discuss how to discretize (3.2) in time. We first observe that, since $\partial_t \rho = 0$, system (3.2) essentially reduces to a coupled system for the velocity \mathbf{v} and the potential φ ,

$$(3.3) \quad \begin{cases} \partial_t \mathbf{v} = -\nabla \varphi + \mathbf{v} \times \boldsymbol{\Omega}, \\ \partial_t (-\Delta \varphi) = -\alpha \nabla \cdot (\rho \mathbf{v}). \end{cases}$$

The rate of change of the total mechanical energy \mathcal{E} is then determined by

$$(3.4) \quad \partial_t \mathcal{E} = -\rho \mathbf{v} \cdot \nabla \varphi$$

and simply equates to the rate of change of the kinetic energy. In order to accommodate different IMEX time-stepping techniques, we now discretize (3.3) in time with a θ -scheme, where $\theta = 1$ recovers a backward Euler step and $\theta = 1/2$ is the Crank-Nicolson scheme.

$$(3.5) \quad \begin{cases} \mathbf{v}^{n+\theta} = \mathbf{v}^n - \theta \tau_n \nabla \varphi^{n+\theta} + \theta \tau_n \mathbf{v}^{n+\theta} \times \boldsymbol{\Omega}, \\ -\Delta \varphi^{n+\theta} = -\Delta \varphi^n - \theta \tau_n \alpha \nabla \cdot (\rho^n \mathbf{v}^{n+\theta}), \\ \mathbf{v}^{n+1} = \frac{1}{\theta} \mathbf{v}^{n+\theta} - \frac{1-\theta}{\theta} \mathbf{v}^n, \\ \varphi^{n+1} = \frac{1}{\theta} \varphi^{n+\theta} - \frac{1-\theta}{\theta} \varphi^n. \end{cases}$$

Note that the first two lines of (3.5) correspond with a coupled system, while the last two lines are just an extrapolation step.

LEMMA 3.2 (Semi-discrete parabolic energy balance). *The semi-discrete system (3.5) admits an energy balance:*

$$\begin{aligned}
(3.6) \quad & \frac{1}{2\alpha} \int_D \alpha \rho_n |\mathbf{v}^{n+1}|_{\ell^2}^2 + |\nabla \varphi^{n+1}|_{\ell^2}^2 \, dx \\
& + \left(\theta - \frac{1}{2} \right) \frac{1}{2\alpha} \int_D \alpha \rho_n |\mathbf{v}^{n+1} - \mathbf{v}^n|_{\ell^2}^2 + |\nabla \varphi^{n+1} - \nabla \varphi^n|_{\ell^2}^2 \, dx \\
& = \frac{1}{2\alpha} \int_D \alpha \rho_n |\mathbf{v}^n|_{\ell^2}^2 + |\nabla \varphi^n|_{\ell^2}^2 \, dx \\
& + \tau_n \int_{\partial D} \left\{ \frac{1}{\alpha} \frac{\nabla \varphi^{n+\theta} - \nabla \varphi^n}{\theta \tau_n} - \rho^n \mathbf{v}^{n+\theta} \right\} \cdot \mathbf{n}_{\partial D} \varphi^{n+\theta} \, do_x.
\end{aligned}$$

Proof. Test the first equation of (3.5) with $\theta^{-1} \varphi^n \mathbf{v}^{n+\theta}$ and the second equation with $(\alpha \theta)^{-1} \varphi^{n+\theta}$. Then, the identity follows by integration by parts and observing that the following algebraic *polarization* identity holds true:

$$\frac{1}{\theta} (\theta a + (1 - \theta)b, \theta a + (1 - \theta)b - b) = \frac{1}{2} (|a|^2 - |b|^2) + \left(\theta - \frac{1}{2} \right) |a - b|^2. \quad \square$$

Following the general principle discussed in [40, Sec. 3.2], we now transform the coupled system (3.5) into a lower triangular form that allows us to first solve for the new potential $\varphi^{n+\theta}$ and then compute the new velocity field $\mathbf{v}^{n+\theta}$:

$$(3.7) \quad \begin{cases} -\Delta \varphi^{n+\theta} - \theta^2 \tau_n^2 \alpha \nabla \cdot (\rho^n \mathcal{B}_{n,\theta}^{-1} \nabla \varphi^{n+\theta}) = -\Delta \varphi^n - \theta \tau_n \alpha \nabla \cdot (\rho^n \mathcal{B}_{n,\theta}^{-1} \mathbf{v}^n), \\ \mathbf{v}^{n+\theta} = \mathcal{B}_{n,\theta}^{-1} (\mathbf{v}^n - \theta \tau_n \nabla \varphi^{n+\theta}), \end{cases}$$

where $\mathcal{B}_{n,\theta} : \mathbb{R}^d \rightarrow \mathbb{R}^d$ is defined by

$$(3.8) \quad \mathcal{B}_{n,\theta} \mathbf{v} := \mathbf{v} - \theta \tau_n \mathbf{v} \times \boldsymbol{\Omega} \quad \text{for } \mathbf{v} \in \mathbb{R}^d.$$

Note that $\det(\mathcal{B}_{n,\theta}) = 1 + \theta^2 \tau_n^2 |\boldsymbol{\Omega}|_{\ell^2}^2 = 1 + \theta^2 \tau_n^2 \omega_c^2$, moreover, the inverse can be written as

$$\mathcal{B}_{n,\theta}^{-1} \mathbf{v} = \frac{\mathbf{v} + \theta \tau_n \mathbf{v} \times \boldsymbol{\Omega} + \theta^2 \tau_n^2 (\mathbf{v} \cdot \boldsymbol{\Omega}) \boldsymbol{\Omega}}{1 + \theta^2 \tau_n^2 |\boldsymbol{\Omega}|_{\ell^2}^2}.$$

We note in passing that formulation (3.7)-(3.8) is closely related to what is usually known as static condensation in the finite element literature [48]. Here, we set $\mathbf{v} \cdot \boldsymbol{\Omega} = 0$ in the 2D case ($d = 2$), consistent with our convention of using a transverse magnetic configuration. We make the following observation for the bilinear form arising from the weak formulation of (3.7).

LEMMA 3.3 (Well posedness). *Suppose that $\rho^n \in L^\infty(D)$. Then, the bilinear form*

$$a_{n,\theta}(\varphi, \psi) := (\nabla \varphi, \nabla \psi)_{L^2(D)^d} + \theta^2 \tau_n^2 \alpha (\rho^n \mathcal{B}_{n,\theta}^{-1} \nabla \varphi, \nabla \psi)_{L^2(D)^d}$$

is coercive and bounded on $H^1(D)$; and the boundedness constant C formally scales with $C = \mathcal{O}(\tau_n^2 \omega_p^2)$.

It is of interest to discuss briefly in what form subsystem (3.5) can be made compatible with the magnetic drift limit (2.7). Notably, mathematical results related to the convergence of limiting processes, e.g., by weak-defect measure limits [24], raise the uncomfortable question whether such an endeavour is actually meaningful numerically. Nevertheless, we report the following result:

LEMMA 3.4 (Compatibility with magnetic drift limit). *Suppose that at t_n the state $[\rho^n, \mathbf{v}^n, \varphi^n]$ satisfies the following algebraic conditions:*

$$\nabla \varphi^n \perp \Omega, \quad \mathbf{v}^n = -\frac{\nabla \varphi^n \times \Omega}{|\Omega|_{\ell^2}^2}, \quad \nabla \cdot (\rho^n \mathbf{v}^n) = 0.$$

Then, the solution to (3.5) satisfies $\mathbf{v}^{n+\theta} = \mathbf{v}^n$ and $\varphi^{n+\theta} = \varphi^n$, i.e., the algebraic conditions are preserved.

Proof. We start by rewriting the first equation of (3.7) by subtracting the same terms for φ^n that appear on the left-hand side of the equation. Using the first and second assumption to manipulate the right hand side shows:

$$\begin{aligned} -\Delta \{\varphi^{n+\theta} - \varphi^n\} - \theta^2 \tau_n^2 \alpha \nabla \cdot (\rho^n \mathcal{B}_{n,\theta}^{-1} \nabla \{\varphi^{n+\theta} - \varphi^n\}) \\ = -\theta \tau_n \alpha \nabla \cdot (\rho^n \mathcal{B}_{n,\theta}^{-1} \mathbf{v}^n) + \theta^2 \tau_n^2 \alpha \nabla \cdot (\rho^n \mathcal{B}_{n,\theta}^{-1} \nabla \varphi^n) \\ = -\theta \tau_n \alpha \nabla \cdot \left(\rho^n \mathcal{B}_{n,\theta}^{-1} \left\{ \mathbf{v}^n + \theta \tau_n \frac{\nabla \varphi^n \times \Omega}{|\Omega|_{\ell^2}^2} \times \Omega \right\} \right) \\ = -\theta \tau_n \alpha \nabla \cdot (\rho^n \mathcal{B}_{n,\theta}^{-1} \mathcal{B}_{n,\theta} \mathbf{v}^n) = 0. \end{aligned}$$

The left-hand side is a coercive operator, thus $\varphi^{n+\theta} = \varphi^n$. Next, using the second algebraic condition, the second equation of (3.7) can be rewritten as follows:

$$\mathcal{B}_{n,\theta} \{\mathbf{v}^{n+\theta} - \mathbf{v}^n\} = \theta \tau_n (\nabla \varphi^{n+\theta} - \nabla \varphi^n) = 0,$$

implying that $\mathbf{v}^{n+\theta} = \mathbf{v}^n$. \square

Remark 3.5 (Asymptotic compatibility with equilibrium solutions). As an immediate consequence, we observe that any flow configuration with a barotropic equation of state in the regime of *negligible pressure* and with a rotationally symmetric density profile (that only depends on the radius r in cylindrical coordinates) is a (almost) stationary solution to the Euler-Poisson system (on the continuous and semidiscrete level):

$$\rho = \rho(r), \quad p = p(\rho) \approx 0, \quad \mathbf{v}^n = -\frac{\nabla \varphi^n \times \Omega}{|\Omega|_{\ell^2}^2}.$$

4. A fully discrete structure-preserving discretization. We now describe a spatial discretization of (3.7) that maintains the crucial equivalence of (3.5) and (3.7) on a fully discrete level. This in turn enables us to establish discrete counterparts of Lemmas 3.2 and 3.4. We start by introducing the finite element spaces and a lumped inner product. Then, we discuss the fully discrete system.

4.1. Finite element spaces. Let \mathbb{Q}_1 denote the space of d -variable polynomials of degree at most 1 in each variable, and let $\widehat{K} = [0, 1]^d$ denote the reference cell. Let \mathcal{T}_h be a *shape and form regular* mesh consisting of quadrilateral (for $d = 2$) or hexahedral (for $d = 3$) cells K , covering the domain D , and obtained from a diffeomorphic mapping $\mathbf{T}_K : \widehat{K} \rightarrow K$. We then introduce a discontinuous and a continuous finite element space as follows:

$$\begin{aligned} \mathbb{V}_h &:= \{z_h \in L^2(D) : z_h \circ \mathbf{T}_K \in \mathbb{Q}_1 \text{ for all } K \in \mathcal{T}_h\}, \\ (4.1) \quad \mathbb{H}_h &:= \{\psi_h \in \mathcal{C}^0(D) : \psi_h \circ \mathbf{T}_K \in \mathbb{Q}_1 \text{ for all } K \in \mathcal{T}_h\}. \end{aligned}$$

Let $\{\mathbf{x}_i\}_{i=1}^N$ denote the vertices of \mathcal{T}_h . Let $\{\phi_{i,K}\}$ be the nodal basis of the discontinuous space \mathbb{V}_h . Here, we choose to index a basis function by the index i of their support point \mathbf{x}_i and the cell K where they are located. Correspondingly, let $\{\chi_i\}$ be the nodal basis of the continuous space \mathbb{H}_h with support points \mathbf{x}_i .

The mapping $\mathbf{T}_K : \hat{K} \rightarrow K$ is not assumed to be affine. Therefore, it is *not* necessarily true that $\nabla \mathbb{H}_h \subset \mathbb{V}_h^3$, which on the semidiscrete level is a crucial property to establish equivalence between (3.5) and (3.7). Furthermore, in order to connect a fully discrete energy balance to the energy balance of the (algebraic) approximation of the hyperbolic subsystem, we need to extract the kinetic energy as an algebraic sum over collocated point values in support points rather than an integral [40]. For this reason we need to make use of a carefully constructed lumped inner product with corresponding nodal interpolant. We define

DEFINITION 4.1 (Lumped inner product). *For $\varphi_h, \psi_h \in \mathbb{V}_h$ we set*

$$(4.2) \quad \langle \varphi_h, \psi_h \rangle_h := \sum_{j=1}^N \sum_{K \in \mathcal{T}_h} m_{j,K} \varphi_h|_K(\mathbf{x}_j) \psi_h|_K(\mathbf{x}_j)$$

where $m_{j,K} := \int_K \phi_{j,K}(\mathbf{x}) dx$ is an element of the lumped mass matrix. The corresponding norm shall be denoted by $\|\varphi_h\|_h := \sqrt{\langle \varphi_h, \varphi_h \rangle_h}$.

We observe that $\langle \varphi_h, \psi_h \rangle_h$ is a proper inner product on \mathbb{H}_h approximating the $L^2(D)$ inner product. We extend the inner product to vector-valued functions $\varphi_h, \psi_h \in \mathbb{V}_h^d$ by setting

$$\langle \varphi_h, \psi_h \rangle_h := \sum_{j=1}^N \sum_{K \in \mathcal{T}_h} m_{j,K} \varphi_h|_K(\mathbf{x}_j) \cdot \psi_h|_K(\mathbf{x}_j).$$

The corresponding nodal interpolant $I_h : \mathcal{C}^0(\mathcal{T}_h)^d \rightarrow \mathbb{V}_h^d$ is given by

$$(4.3) \quad (I_h \varphi)(\mathbf{x}) := \sum_{j=1}^N \sum_{K \in \mathcal{T}_h} \varphi|_K(\mathbf{x}_j) \phi_{j,K}(\mathbf{x}).$$

By construction, it holds true that

$$\langle I_h \varphi, \psi \rangle_h = \langle \varphi, I_h \psi \rangle_h = \langle \varphi, \psi \rangle_h \quad \text{for all } \varphi, \psi \in \mathcal{C}^0(\mathcal{T}_h)^d.$$

4.2. Assumptions on the hyperbolic solver. We now summarize our structural assumptions on the discretization of the hyperbolic subsystem. For the sake of completeness, we outline some implementation details of the hyperbolic solver used in our numerical computations in Appendix B. In general, we make the following assumptions on the hyperbolic update procedure.

We assume that all components of the hyperbolic state approximation $\mathbf{u}_h^n = [\rho_h^n, \mathbf{m}_h^n, \mathcal{E}_h^n]$ for time t_n are discretized using the scalar-valued, discontinuous finite element space \mathbb{V}_h introduced above:

$$\mathbf{u}_h^n(\mathbf{x}) = \sum_{j=1}^N \sum_{K \in \mathcal{T}_h} \mathbf{U}_{i,K}^n \phi_{i,K}(\mathbf{x}),$$

where $\mathbf{U}_{i,K}^n = [\rho_i^n, \mathbf{m}_i^n, \mathcal{E}_i^n] \in \mathbb{R}^{d+2}$. Let \mathbf{u}_h^{n+1} be the discrete update computed with the hyperbolic solver for time t_{n+1} . The hyperbolic update shall maintain an

admissible set, this is to say that

$$\mathbf{U}_{i,K}^n \in \mathcal{A} \text{ for all } i \leq \mathcal{N}, K \in \mathcal{T}_h \text{ implies } \mathbf{U}_{i,K}^{n+1} \in \mathcal{A} \text{ for all } i \leq \mathcal{N}, K \in \mathcal{T}_h,$$

where $\mathcal{A} = \{\mathbb{R}^{d+2} \mid \rho > 0 \text{ and } e(\mathbf{u}) > 0\}$ for the case of the full Euler equations with covolume equation of state. For the case of barotropic equation of state, when the energy equation is not part of the system, admissibility reduces to positivity of the density, $\mathcal{A} = \{\mathbb{R}^{d+1} \mid \rho > 0\}$.

Conservation. Neglecting the influence of boundary conditions, we assume that the hyperbolic solver is conservative, i. e.,

$$\sum_{j=1}^{\mathcal{N}} \sum_{K \in \mathcal{T}_h} m_{i,K} \mathbf{U}_{i,K}^{n+1} = \sum_{j=1}^{\mathcal{N}} \sum_{K \in \mathcal{T}_h} m_{i,K} \mathbf{U}_{i,K}^n.$$

Entropy inequalities. Finally, we assume that the hyperbolic solver maintains in some sense a global entropy inequality: Selecting a suitable entropy η and neglecting the influence of boundary conditions,

$$(4.4) \quad \sum_{j=1}^{\mathcal{N}} \sum_{K \in \mathcal{T}_h} m_{i,K} \eta(\mathbf{u}_{i,K}^{n+1}) \leq \sum_{j=1}^{\mathcal{N}} \sum_{K \in \mathcal{T}_h} m_{i,K} \eta(\mathbf{u}_{i,K}^n).$$

4.3. Fully discrete source update. We are now in a position to introduce a fully discrete counterpart to (3.7). We proceed as follows.

DEFINITION 4.2 (Fully discrete source update). *Given discrete $\rho_h^n \in \mathbb{V}_h$, $\mathbf{v}_h^n \in \mathbb{V}_h^d$, $\varphi_h^n \in \mathbb{H}_h$ at time t_n , compute approximations $\mathbf{v}_h^{n+1} \in \mathbb{V}_h^d$ and $\varphi_h^{n+1} \in \mathbb{H}_h$ at time $t_{n+1} = t_n + \tau_n$ as follows:*

$$(4.5) \quad \left\{ \begin{array}{l} a_h^{n,\theta}(\varphi_h^{n+\theta}, \psi_h) = (\nabla \varphi_h^n, \nabla \psi_h) + \theta \tau_n \alpha \langle \rho_h^n \mathcal{B}_{n,\theta}^{-1} \mathbf{v}_h^n, \nabla \psi_h \rangle_h, \quad \forall \psi_h \in \mathbb{H}_h, \\ \langle \mathbf{v}_h^{n+\theta}, \mathbf{z}_h \rangle_h = \langle \mathcal{B}_n^{-1}(\mathbf{v}_h^n - \theta \tau_n \nabla \varphi_h^{n+\theta}), \mathbf{z}_h \rangle_h, \quad \forall \mathbf{z}_h \in \mathbb{V}_h^d, \\ \theta \mathbf{v}^{n+1} = \mathbf{v}^{n+\theta} - (1 - \theta) \mathbf{v}^n, \\ \theta \varphi^{n+1} = \varphi^{n+\theta} - (1 - \theta) \varphi^n. \end{array} \right.$$

Here, we have introduced the discrete bilinear form

$$(4.6) \quad a_h^{n,\theta}(\varphi_h, \psi_h) := (\nabla \varphi_h, \nabla \psi_h) + \theta^2 \tau_n^2 \alpha \langle \rho_h^n \mathcal{B}_{n,\theta}^{-1} \nabla \varphi_h, \nabla \psi_h \rangle_h.$$

4.4. Well-posedness and structure preservation. We now establish that, for sufficiently regular mesh families $\{\mathcal{T}_h\}_h$, the bilinear form $a_{h>0}^{n,\theta}$ is uniformly coercive and bounded with a constant independent of ω_c and essentially only depending on $\tau_n^2 \omega_p^2$. To this end, we require that the selected mesh family $\{\mathcal{T}_h\}_{h \geq 0}$ is sufficiently regular such that the following assumption holds true on the approximation quality of the lumped inner product.

Assumption 4.3. There exist constants $C, s > 0$ such that, for all $h > 0$,

$$|\|\mathbf{v}_h\|_h - \|\mathbf{v}_h\|_{\mathbf{L}^2(D)}| \leq C h^s \|\mathbf{v}_h\|_{\mathbf{L}^2(D)} \quad \text{for all } \mathbf{v}_h \in \mathbb{V}_h^d.$$

PROPOSITION 4.4 (Coercivity and boundedness). *Suppose that Assumption 4.3 holds true. Then, there exists a constant c independent of h (and ω_p), such that for*

all $\varphi_h, \psi_h \in \mathbb{V}_h^d$:

$$a_h^{n,\theta}(\varphi_h, \varphi_h) \geq \|\nabla \varphi_h\|_{\mathbf{L}^2(D)}^2,$$

$$|a_h^{n,\theta}(\varphi_h, \psi_h)| \leq (1 + c\tau_n^2\alpha\|\rho_h^n\|_{h,\infty})\|\nabla \varphi_h\|_{\mathbf{L}^2(D)}\|\nabla \psi_h\|_{\mathbf{L}^2(D)}.$$

Here, $\|\rho_h^n\|_{h,\infty}$ denotes the largest value of $|\rho_h^n|$ obtained in the support points of \mathbb{V}_h .

Proof. The first inequality follows directly from the definition of $a_h^{n,\theta}$ and the inverse (3.2),

$$\begin{aligned} a_h^{n,\theta}(\varphi_h, \varphi_h) &= \|\nabla \varphi_h\|_{\mathbf{L}^2(D)}^2 \\ &+ \frac{\theta^2\tau_n^2\alpha}{(1 + \theta^2\tau_n^2|\boldsymbol{\Omega}|_{\ell^2}^2)} \left\{ \langle \rho_h^n \nabla \varphi_h, \nabla \varphi_h \rangle_h + \tau_n^2 \langle \rho_h^n \nabla \varphi_h \cdot \boldsymbol{\Omega}, \nabla \varphi_h \cdot \boldsymbol{\Omega} \rangle_h \right\} \\ &\geq \|\nabla \varphi_h\|_{\mathbf{L}^2(D)}^2. \end{aligned}$$

This establishes the first inequality. For the second inequality we estimate similarly:

$$\begin{aligned} (4.7) \quad |a_h^{n,\theta}(\varphi_h, \psi_h)| &\leq \|\nabla \varphi_h\|_{\mathbf{L}^2(D)}\|\nabla \psi_h\|_{\mathbf{L}^2(D)} \\ &+ \theta^2\tau_n^2\alpha\|\rho_h^n\|_{h,\infty} \frac{1 + 2\tau_n|\boldsymbol{\Omega}|_{\ell^2} + \tau_n^2|\boldsymbol{\Omega}|_{\ell^2}^2}{1 + \tau_n^2|\boldsymbol{\Omega}|_{\ell^2}^2} \|\nabla \varphi_h\|_h\|\nabla \psi_h\|_h, \end{aligned}$$

which combined with Assumption 4.3 establishes the result. \square

We note

COROLLARY 4.5. *The fully discrete update (4.5) is well posed.*

Now, we establish the main result of this section.

PROPOSITION 4.6 (Fully discrete parabolic energy balance). *Writing*

$$\rho_h^\nu =: \sum_{j=1}^N \sum_{K \in \mathcal{T}_h} \rho_{j,K}^\nu \phi_{j,K}, \quad \mathbf{v}_h^\nu =: \sum_{j=1}^N \sum_{K \in \mathcal{T}_h} \mathbf{v}_{j,K}^\nu \phi_{j,K},$$

for $\nu = n, n + \theta$, the fully discrete system (4.5) admits an energy balance:

$$\begin{aligned} (4.8) \quad &\sum_{j=1}^N \sum_{K \in \mathcal{T}_h} \frac{1}{2} m_{j,K} \rho_{j,K}^n |\mathbf{v}_{j,K}^{n+1}|_{\ell^2}^2 + \frac{1}{2\alpha} \int_D |\nabla \varphi_h^{n+1}|_{\ell^2}^2 dx \\ &+ (\theta - \frac{1}{2}) \left\{ \sum_{j=1}^N \sum_{K \in \mathcal{T}_h} \frac{1}{2} m_{j,K} \rho_{j,K}^n |\mathbf{v}_{j,K}^{n+1} - \mathbf{v}_{j,K}^n|_{\ell^2}^2 + \frac{1}{2\alpha} \int_D |\nabla \varphi_h^{n+1} - \nabla \varphi_h^n|_{\ell^2}^2 dx \right\} \\ &= \sum_{j=1}^N \sum_{K \in \mathcal{T}_h} \frac{1}{2} m_{j,K} \rho_{j,K}^n |\mathbf{v}_{j,K}^n|_{\ell^2}^2 + \frac{1}{2\alpha} \int_D |\nabla \varphi_h^n|_{\ell^2}^2 dx. \end{aligned}$$

Proof. We first observe that the following identity holds for any $\mathbf{v}_h, \mathbf{z}_h \in \mathcal{C}^0(\mathcal{T}_h)^d$ and any $\mathcal{A} \in \mathbb{R}^{d \times d}$:

$$\langle \mathcal{A} \mathbf{v}_h, \mathbf{z}_h \rangle_h = \langle \mathbf{v}_h, \mathcal{A}^\top \mathbf{z}_h \rangle_h,$$

where \mathcal{A}^\top is the transpose of \mathcal{A} . Thus, by replacing \mathbf{z}_h with $\mathcal{B}_{n,\theta}^\top \mathbf{z}_h$ in the second equation of (4.5) and using (3.8) and the third equation in (4.5), we obtain the identity

$$\langle \mathbf{v}_h^{n+\theta}, \mathbf{z}_h \rangle_h = \langle \mathbf{v}_h^n, \mathbf{z}_h \rangle_h - \theta \tau_n \langle \nabla \varphi_h^{n+\theta}, \mathbf{z}_h \rangle_h + \theta \tau_n \langle \mathbf{v}_h^{n+\theta} \times \boldsymbol{\Omega}, \mathbf{z}_h \rangle_h.$$

Next, due to the use of the lumped inner product, the second equation of (4.5) also holds true when scaling the test function with the density field:

$$\langle \mathbf{v}_h^{n+\theta}, \rho_h^n \mathbf{z}_h \rangle_h = \langle \mathcal{B}_n^{-1} (\mathbf{v}_h^n - \theta \tau_n \nabla \varphi_h^{n+\theta}), \rho_h^n \mathbf{z}_h \rangle_h.$$

Rearranging the first equation of (4.5) and substituting the above identities recovers a symmetric version of the update:

$$(4.9) \quad \begin{cases} (\nabla \varphi_h^{n+\theta}, \nabla \psi_h) = (\nabla \varphi_h^n, \nabla \psi_h) + \theta \tau_n \alpha \langle \rho_h^n \mathbf{v}_h^{n+\theta}, \nabla \psi_h \rangle_h, & \forall \psi_h \in \mathbb{H}_h, \\ \langle \mathbf{v}_h^{n+\theta}, \mathbf{z}_h \rangle_h = \langle \mathbf{v}_h^n - \theta \tau_n \nabla \varphi_h^{n+\theta} + \theta \tau_n \mathbf{v}_h^{n+\theta} \times \boldsymbol{\Omega}, \mathbf{z}_h \rangle_h, & \forall \mathbf{z}_h \in \mathbb{V}_h^d. \end{cases}$$

The result now follows similarly to the proof of Lemma 3.2 by testing with

$$\psi_h := (\alpha \theta)^{-1} \varphi_h^{n+\theta}, \quad \text{and} \quad \mathbf{z}_h := \theta^{-1} I_h(\rho_h^n \mathbf{v}_h^{n+\theta}). \quad \square$$

We are now in a position to formulate the full source update procedure.

DEFINITION 4.7 (Full source update procedure on conserved states). *Given a conserved state $[\rho_h^n, \mathbf{m}_h^n, \mathcal{E}_h^n]^T \in \mathbb{V}_h^{d+2}$ and $\varphi_h^n \in \mathbb{H}_h$ at time t_n and a given new time $t_{n+1} = t_n + \tau_n$ an update is computed as follows:*

- Compute a velocity field $\mathbf{v}_h^n \in \mathbb{V}_h^d$ and internal energy per unit volume $\varepsilon_h^n \in \mathbb{V}_h$ by setting the corresponding nodal degrees of freedom to

$$\mathbf{v}_{i,K}^n := \mathbf{m}_{i,K}^n / \rho_{i,K}^n, \quad \varepsilon_{i,K}^n := \mathcal{E}_{i,K}^n - \frac{1}{2} |\mathbf{m}_{i,K}^n|_{\ell^2}^2 / \rho_{i,K}^n.$$

- Compute an update $\mathbf{v}_h^{n+1} \in \mathbb{V}_h^d$ and $\varphi_h^{n+1} \in \mathbb{H}_h$ for time t_{n+1} by solving (4.5).
- Reconstruct the momentum $\mathbf{m}_h^{n+1} \in \mathbb{V}_h^d$ and total mechanical energy $\mathcal{E}_h^{n+1} \in \mathbb{V}_h$ by setting the corresponding nodal degrees of freedom to

$$\mathbf{m}_{i,K}^{n+1} := \rho_{i,K}^n \mathbf{m}_{i,K}^n, \quad \mathcal{E}_{i,K}^{n+1} := \varepsilon_{i,K}^n + \frac{1}{2} \rho_{i,K}^n |\mathbf{v}_{i,K}^{n+1}|_{\ell^2}^2.$$

COROLLARY 4.8. *The update procedure outlined in Definition 4.7 maintains an energy inequality, i. e.,*

$$(4.10) \quad \begin{aligned} & \sum_{j=1}^N \sum_{K \in \mathcal{T}_h} \frac{1}{2} m_{j,K} \mathcal{E}_{i,K}^{n+1} + \frac{1}{2\alpha} \int_D |\nabla \varphi_h^{n+1}|_{\ell^2}^2 dx \\ & \leq \sum_{j=1}^N \sum_{K \in \mathcal{T}_h} \frac{1}{2} m_{j,K} \mathcal{E}_{i,K}^n + \frac{1}{2\alpha} \int_D |\nabla \varphi_h^n|_{\ell^2}^2 dx, \end{aligned}$$

with equality holding for the case of $\theta = 1/2$. Furthermore, by construction the density $\rho_{i,K}^n$ and the internal energy per unit volume $\varepsilon_{i,K}^n$ are not modified.

4.5. Restart strategies for the Gauß law. The numerical scheme for the source update (4.5) does not preserve the Gauß law. That is, a discrete counterpart of $-\Delta \varphi = \alpha \rho$ does not necessarily hold true any more for the final update $\{\rho_h^{n+1}, \varphi_h^{n+1}\}$ obtained after a Strang split (Definition 3.1), or, equivalently, a high-order IMEX

step. In this section, we follow a strategy outlined in [40, Section 4] to postprocess the potential φ_h^{n+1} in order to reestablish a discrete Gauß law between φ_h^{n+1} and ρ_h^{n+1} . One possible restart strategy is to fully reset the potential φ_h^{n+1} at the end of the Strang (or IMEX) step:

DEFINITION 4.9 (Full Gauß law restart). *Let $\{\rho_h^{n+1}, \varphi_h^{n+1}\}$ be the final density and potential obtained after a full strang split (Definition 3.1), or an equivalent IMEX update procedure. Then, compute $\tilde{\varphi}_h^{n+1} \in \mathbb{H}_h$ satisfying the discrete Gauß law:*

$$(4.11) \quad (\nabla \tilde{\varphi}_h^{n+1}, \nabla \omega_h) = \alpha \langle \rho_h^{n+1}, \omega_h \rangle_h \quad \text{for all } \omega_h \in \mathbb{H}_h,$$

and set $\varphi_h^{n+1} \leftarrow \tilde{\varphi}_h^{n+1}$.

This process comes at the expense of losing the energy stability established in Proposition 4.6. Fortunately, the next result shows that the deviation introduced by this restart strategy is small.

PROPOSITION 4.10. *Assume that the hyperbolic update is at least first-order accurate in time and space and subject to a hyperbolic CFL condition $\tau_n = \mathcal{O}(h)$. Then, introducing the Gauß law residual $\mathcal{R}_h^{n+1}[\omega_h] = \alpha \langle \rho_h^{n+1}, \omega_h \rangle_h - (\nabla \varphi_h^{n+1}, \nabla \omega_h)$ we have that*

$$(4.12) \quad \|\mathcal{R}_h^{n+1}[\cdot] - \mathcal{R}_h^n[\cdot]\|_{op} = \alpha \mathcal{O}(h^2 + h^{1+s}),$$

where s is the constant introduced in Assumption 4.3. The result can be improved to $\|\mathcal{R}_h^{n+1}[\cdot] - \mathcal{R}_h^n[\cdot]\|_{op} = \alpha \mathcal{O}(h^3 + h^{1+s})$ for the case of a Strang split with a hyperbolic update of at least second order and a source update with $\theta = 1/2$.

Proof. Let $\{[\rho_h^n, \mathbf{m}_h^n, \mathcal{E}_h^n], \varphi_h^n\}$ be the computed state at time t_n and let the discrete state $\{[\rho_h^{n+1}, \mathbf{m}_h^{n+1}, \mathcal{E}_h^{n+1}], \varphi_h^{n+1}\}$ be the final update obtained after a full Strang split (Definition 3.1). Let $\hat{\rho}_h^n$ be the intermediate density update with which the source update is performed in the Strang split, and let $\check{\mathbf{v}}_h^{n+\theta}$ be the intermediate velocity obtained from the theta scheme for the source update; see Definition 3.1 and (4.5). We recall that $\varphi^{n+\theta} = \theta \varphi^{n+1} + (1-\theta) \varphi^n$ and by slight abuse of notation we also introduce a density $\rho^{n+\theta} := \theta \rho^{n+1} + (1-\theta) \rho^n$. Recalling (4.9), we then have

$$\begin{aligned} \mathcal{R}_h^{n+\theta}[\omega_h] - \mathcal{R}_h^n[\omega_h] &= \alpha \langle \rho_h^{n+\theta} - \rho_h^n, \omega_h \rangle_h - (\nabla \varphi_h^{n+\theta} - \nabla \varphi_h^n, \nabla \omega_h) \\ &= \alpha \langle \rho_h^{n+\theta} - \rho_h^n, \omega_h \rangle_h - \theta \tau_n \alpha \langle \hat{\rho}_h^n \check{\mathbf{v}}_h^{n+\theta}, \nabla \omega_h \rangle_h, \end{aligned}$$

We observe that the right-hand side of the above equation resembles a discretization of the balance of mass equation $\partial_t \rho + \nabla \cdot \mathbf{m} = 0$ with a θ time stepping scheme:

$$\langle \tilde{\rho}_h^{n+\theta}, \omega_h \rangle_h + \theta \tau_n \alpha \langle \tilde{\rho}_h^{n+\theta} \check{\mathbf{v}}_h^{n+\theta}, \nabla \omega_h \rangle = \langle \rho_h^n, \omega_h \rangle_h,$$

where $\tilde{\rho}_h^{n+\theta}$ is a formal density update with a given (interpolatory) velocity field $\check{\mathbf{v}}_h^{n+\theta}$ at time $t_{n+\theta}$. From our assumptions on the hyperbolic solver we now make the claim that $\|\tilde{\rho}_h^{n+\theta} - \rho_h^{n+\theta}\| = \mathcal{O}(\tau_n^2) = \mathcal{O}(h^2)$, which would need to be verified in detail for the concrete chosen method. The switch between the lumped inner product and the full L^2 -product introduces an additional error of the order $\mathcal{O}(\tau_n h^s) = \mathcal{O}(h^{1+s})$. A more careful analysis for the case $\theta = 1/2$ establishes the improved result $\mathcal{O}(h^3 + h^{1+s})$. \square

COROLLARY 4.11. *Let $\tilde{\varphi}_h^{n+1}$ be the solution to (4.11) and φ_h^{n+1} the solution to (4.5). Now, observing that $\mathcal{R}_h^n[\tilde{\varphi}_h^n - \varphi_h^n] = \|\nabla \tilde{\varphi}_h^n - \nabla \varphi_h^n\|_{L^2(\Omega)^d}^2$ and using (4.12) in a*

telescopic sum establishes

$$\begin{aligned}\|\nabla \tilde{\varphi}_h^n - \nabla \varphi_h^n\|_{L^2(\Omega)^d} &= (t_n - t_0) \alpha \mathcal{O}(h + h^s), \\ \|\nabla \tilde{\varphi}_h^{n+1}\|_{L^2(\Omega)^d}^2 - \|\nabla \varphi_h^{n+1}\|_{L^2(\Omega)^d}^2 &= (t_n - t_0) \alpha \mathcal{O}(h + h^s).\end{aligned}$$

Similarly, higher-order convergence of $\mathcal{O}(h^2 + h^s)$ holds true for the case of a Strang split with a hyperbolic update of at least second order and a source update with $\theta = 1/2$.

It is desirable to reestablish a discrete energy balance again after performing restart [40, 47, 48]. This can be achieved via an artificial relaxation approach by lowering the kinetic energy appropriately [40]. We summarize:

DEFINITION 4.12 (Gauß law restart with relaxation). *Let $\{\rho_h^{n+1}, \varphi_h^{n+1}\}$ be the final density and potential obtained after a full strang split (Definition 3.1), and let $\tilde{\varphi}_h^{n+1} \in \mathbb{H}_h$ be the solution to (4.11). Introduce*

$$\begin{aligned}\delta \mathcal{E}^{n+1} &:= \frac{1}{2\alpha} \left(\|\nabla \tilde{\varphi}_h^{n+1}\|^2 - \|\nabla \varphi_h^{n+1}\|^2 \right) \\ \mathcal{E}_{kin}^{n+1} &:= \sum_i \frac{m_i}{2} \rho_i^n |\mathbf{v}^{n+1}|^2,\end{aligned}$$

and set

$$\varphi_h^{n+1} \leftarrow \tilde{\varphi}_h^{n+1}, \quad \mathbf{m}_i^{n+1} \leftarrow \left\{ 1 - \max \left(0, \frac{\delta \mathcal{E}^{n+1}}{\mathcal{E}_{kin}^{n+1}} \right) \right\}^{1/2} \mathbf{m}_i^n.$$

5. Numerical illustrations. We now present a number of computational results that illustrate the performance of the method (a) on a smooth test case (see Section 5.2, and (b) on a problem in the magnetic drift limit with huge scale separation of the time scales (see Section 5.3).

5.1. Implementational details. The numerical algorithms discussed above have been implemented in the hydrodynamic solver framework `ryujin` [25, 39], which is based on the finite element library `deal.II` [1, 2]. Our implementation is freely available online¹ under a permissible open source license.² Details on the invariant-domain preserving solver for the hyperbolic subsystem (3.1) as discussed in Appendix B can be found in [39], the discretization with discontinuous finite elements is discussed in [36].

The source update operator in turn is discretized with `deal.II`'s matrix-free operator framework [34, 35, 37]: The action of the stiffness matrix described by the bilinear form (4.6) is implemented by repeatedly reconstructing the local stencil of the system matrix whenever a matrix-vector multiplication is performed. We refer the reader to [25] for a related, detailed discussion and cost analysis of the matrix-free operator approach applied to such source systems. We note that the dominant operator in (4.6) is a Laplacian and not a mass matrix, irrespective of the chosen time-step size. This is, for example, in contrast to the parabolic diffusion operator encountered in the compressible Navier-Stokes equations when performing an operator split [25]. In addition, the boundedness constant of (4.6) scales with $\mathcal{O}(\tau_n \omega_p^2)$; see Proposition 4.4. For these reasons we settled on using a geometric multigrid preconditioner with Chebyshev smoother [8, 37]. After careful tuning we observe that solving

¹<https://github.com/conservation-laws/ryujin>

²<https://spdx.org/licenses/Apache-2.0.html>

dofs	δ_h	rate	dofs	δ_h	rate
4096	1.220e+01		4096	3.827e-01	
16384	7.366e+00	0.73	16384	9.118e-02	2.07
65536	4.091e+00	0.85	65536	2.210e-02	2.04
262144	2.165e+00	0.91	262144	5.438e-03	2.02

(a) Low order method

(b) High order method

Table 5.1: Smooth isentropic vortex test: L^1 -error δ_h at the final time t_F for varying global refinement levels and corresponding convergence rate.

the source update (4.5) has the same computational cost as performing the explicit hyperbolic update: For the numerical results discussed below in Section 5.3 we spend around 28 % of the wall time in the source update, while the remaining 72 % of the wall time was split between two hyperbolic updates (with a third order Runge-Kutta scheme), vector transfer and solution output.

5.2. Isentropic vortex. We consider the smooth isentropic vortex solution adapted to the case of the Euler-Poisson system (2.4) with $\Omega = \mathbf{0}$; see [40, Definition 5.2]. The isentropic vortex is an analytic solution of the Euler-Poisson system when the system is augmented with a background density that exactly cancels the effect of the density distribution leading to $\varphi = \text{const}_x$.

With the notation introduced in [40, Definition 5.2] we set $D = [-5, 5]^2$, vortex speed $M = [1, 1]^T$, vortex size $\beta = 5$, and the coupling constant $\alpha = 1$, and magnetic field density $\Omega = \mathbf{0}$. We vortex is initially centered at $[-1, -1]^T \in D$. We approximate the solution to (2.4) using our numerical method on a sequence of successively refined uniform meshes for D . For initial conditions, we interpolate the exact solution at time $t = 0$ to the finite element spaces $\mathbb{V}_h, \mathbb{H}_h$ defined in Section 4.1. For boundary conditions, we impose non-homogeneous Dirichlet boundary conditions using the exact solution.

We construct a low order method by using a forward Euler step for the hyperbolic part and a backward Euler step for the parabolic part (by setting $\theta = 1$ in (4.5)). Correspondingly, a high order method is constructed by combining an optimal, third order explicit Runge-Kutta time stepping scheme [16] for the hyperbolic part and the Crank-Nicoloson scheme (by setting $\theta = 1/2$ in (4.5)) for the source update in a Strang split. The CFL parameter for the hyperbolic update is set to 0.1; see [30]. At the final timestep $t_N := t_F$, we compute the L^1 error

$$\delta_h := \|\rho(t_F) - \rho_h^N\|_{L^1(D)} + \|\mathbf{m}(t_F) - \mathbf{m}_h^N\|_{L^1(D)} + \|\mathcal{E}(t_F) - \mathcal{E}_h^N\|_{L^1(D)}.$$

For our simulations, we set $t_F := 1$. We report the results in Table 5.1 for both, the low-order and high-order method. We recover the expected optimal convergence rates.

5.3. Diocotron instability. Next, we consider the diocotron instability [19, 31, 42, 43, 44, 45, 50] that arises in the context of cold plasma physics. The diocotron instability occurs in an experimental setup where an essentially hollow cylindrical beam of electrons is aligned with an out-of-plane magnetic field. Such an electron profile experiences an instability caused by $\mathbf{E} \times \mathbf{B}$ drift-rotational shear. We use model (2.4)

with the isothermal equation of state $p = \theta\rho$, where $\theta \geq 0$ is the temperature of the plasma. This choice of closure is fundamental for the design a meaningful computational experiment. Since θ is a model parameter and the corresponding thermal sound speed is given by $c = \sqrt{\theta}$, we can make thermal sound speed as small as we wish. For instance, we can make the thermal soundspeed negligible in comparison to material velocity \mathbf{v} . Similarly, with a proper choice parameter α and magnitude of magnetic field $|\boldsymbol{\Omega}|_{\ell^2}$ we can make plasma time scales orders of magnitude larger than the hydrodynamic time-scales. With this setup, we can force, onto the magnetic Euler-Poisson model (2.4), the conditions required to operate in the magnetic-drift regime.

For the test case we set $d = 2$, i.e., the motion of the plasma is restricted to the (x, y) -plane, and the prescribed magnetic field \mathbf{D} is spatially uniform and transverse to the plasma; see Section 2.2. Let $0 < r_0 < r_1 < R$ be three chosen radii and let the computational domain $D \subset \mathbb{R}^2$ be the disc centered in the origin with radius R . Choosing two background densities $0 < \rho_{\min} \ll \rho_{\max}$, introduce an initial density profile given by an annulus of high density with radii r_0 and r_1 :

$$\rho_0(\mathbf{x}) := \begin{cases} \rho_{\min} & \text{for } \|\mathbf{x}\|_{\ell^2} \leq r_0 \text{ or } \|\mathbf{x}\|_{\ell^2} \geq r_1, \\ \rho_{\max} \delta_{\text{per}}(\mathbf{x}) & \text{for } r_0 < \|\mathbf{x}\|_{\ell^2} < r_1. \end{cases}$$

Here,

$$\delta_{\text{per}}(\mathbf{x}) := 1 - \delta + \delta \sin(\ell \arctan(x_2/x_1)),$$

is a small perturbation of the background density with chosen coefficients $0 < \delta \ll 1/2$, and $\ell \in \mathbb{N}$. The initial potential $\varphi_0(\mathbf{x})$ is determined by the Gauß law,

$$-\Delta \varphi_0 = \alpha \rho_0,$$

and the initial velocity $\mathbf{v}_0(\mathbf{x}) = \mathbf{v}_{\text{dr}}$ is given by (2.6). We now introduce a scaling parameter $\beta > 0$ and set $\alpha := \rho_{\max}^{-1} \beta^2$ and $\omega_c := \beta^2$. This results in the following relevant time scales:

$$\omega_c \sim \beta^2, \quad \omega_p \sim \sqrt{\rho_{\max} \alpha} = \beta^1, \quad \omega_d \sim 1.$$

Computational setup and initial values. We now fix the following parameters

$$r_0 = 6, \quad r_1 = 8, \quad R = 16, \quad \rho_{\min} = 10^{-6}, \quad \rho_{\max} = 1, \quad \beta = 10^6, \quad \delta = 0.1,$$

with the goal to perform a series of computations for initial values with differing perturbation modes, $\ell \in \{3, 4, 5\}$. We choose a coarse discretization of D into 12 quadrilaterals and refine the mesh globally to refinement levels $r = 6, 7, 8$ and 9. The corresponding number of degrees of freedom per component, i.e., $\dim \mathbb{V}_h$, are: 196,608 for $r = 6$; 786,432 for $r = 7$; 3,145,728 for $r = 8$; and 12,582,912 for $r = 9$. It holds true that $\dim \mathbb{H}_h \approx \dim \mathbb{V}_h/4$. We first set the initial density by interpolating $\rho_0(\mathbf{x})$:

$$\rho_h^0(\mathbf{x}) := \sum_{j=1}^N \sum_{K \in \mathcal{T}_h} \rho_{j,K}^0 \phi_{j,K}^h(\mathbf{x}), \quad \rho_{j,K}^0 := \rho_0(\mathbf{x}_j).$$

Then we determine the initial potential $\varphi_h^0 \in \mathbb{H}_h$ by solving the discrete Gauß law:

$$(\nabla \varphi_h^0, \nabla \psi_h)_{L^2(D)^d} = \alpha \langle \rho_h^0, \psi_h \rangle_h, \quad \text{for all } \psi_h \in \mathbb{H}_h,$$

and with homogeneous Dirichlet conditions enforced on the discrete boundary of \mathcal{T}_h . Finally, the initial velocity is set to

$$\mathbf{v}_h^0(\mathbf{x}) := \sum_{j=1}^N \sum_{K \in \mathcal{T}_h} \mathbf{v}_{j,K}^0 \phi_{j,K}^h(\mathbf{x}), \quad \mathbf{v}_{j,K}^0 := - \left(\frac{\nabla \varphi_h^0 \times \boldsymbol{\Omega}}{|\boldsymbol{\Omega}|_{\ell^2}^2} \right) \Big|_K (\mathbf{x}_{K,j}).$$

We run the simulations to final time $t_f = 10$, which corresponds to 10 periods of the diocotron timescale. A series of temporal snapshots outlining the time evolution of the solution for refinement level $r = 9$ are shown in Figures 5.1, 5.2, and 5.3. In all simulations, we observe a time-step size on the order of 10^{-3} to 10^{-4} , which is 2 to 3 orders of magnitude larger than the plasma timescale and 8 to 9 orders of magnitude larger than the cyclotron timescale. As the figures show, our method can successfully overstep the fast-moving plasma and cyclotron dynamics while capturing the slow-moving diocotron instabilities. In particular, our numerical results agree well visually with existing results in the literature; cf. [9, Figure 7.21], [10], [38, Figure 9], and [48, Figure 6.1].

Growth rate. Next, we compare the so-called growth rate of each mode to the theoretical growth rate predicted by the linear stability analysis conducted in [13]. In the analysis, under certain assumptions, the electrostatic potential φ is dominated by the amplitude of its unstable ℓ th Fourier mode which grows exponentially in time:

$$(5.1) \quad \varphi(\mathbf{x}, t) \sim \exp(i(\ell \arctan(x_2/x_1) - \omega_\ell t)),$$

where ω_ℓ is a complex frequency, and $\gamma_\ell := \text{Im}(\omega_\ell) > 0$ shall denote the unstable growth rate of the ℓ th mode. The growth rate γ_ℓ can be computed explicitly in terms of the order ℓ of the mode, the diocotron frequency ω_d , and the geometric parameters r_0 , r_1 , and R ; see [13, Equations 26, 27, and 28]. For our setup we obtain the theoretical growth rates

$$\gamma_3 \approx 0.772, \quad \gamma_4 \approx 0.911, \quad \gamma_5 \approx 0.683.$$

In order to compare our computational results to these theoretical predictions, we follow a procedure outlined in [9, Section 7.5] and [10] to numerically estimate the amplitude of the ℓ th Fourier mode of our numerically computed potential: At each timestep t_n we take a discrete Fourier transform of the potential φ_h^n interpreted as a function of polar angle θ for fixed radius $r = r_0$, viz. $\varphi_h^n(\theta, r = r_0)$. Then, we take the modulus of the coefficient corresponding to the ℓ th mode.

Plots of the numerical amplitudes, normalized by their initial value, over time for modes 3, 4, and 5 are shown in Figure 5.4. Since the stability analysis conducted in [13] is obtained from studying a small linearized perturbation of a steady-state solution, we can only hope for our numerical solution to agree with the theoretical growth rate for a small time interval—after an initial startup phase and before strong, nonlinear dynamics dominate. Therefore, for each plot separately, we first visually compare the slope of the numerically computed amplitudes to the slope of the (shifted) theoretical amplitudes $\exp(\gamma_\ell t)$ and determine a region over which we average values for the growth rates. The region are indicated in the plots with square brackets. We then fit an exponential curve to the numerically computed amplitudes for these time ranges. A table of the fitted numerical growth rates $\gamma_{\ell,h}$ and their deviation from the theoretical growth rate γ_ℓ is summarized in Figure 5.4(d) for the three modes.

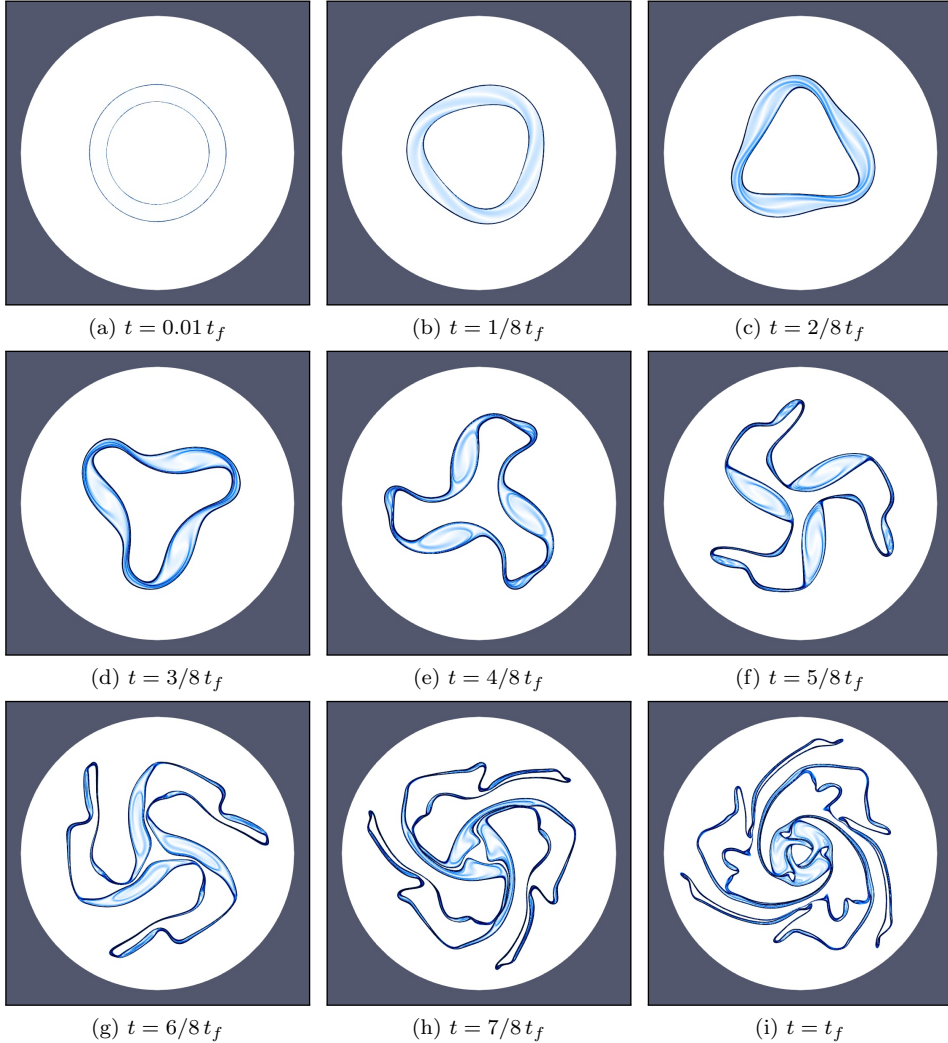


Fig. 5.1: Temporal snapshots of a schlieren plot of the density profile of the third mode diocotron instability test case. Reference computation with no restart on refinement level $r = 9$ amounting to 12,582,912 dG degrees of freedom per component. Here, $t_f = 10$.

6. Conclusion. In this paper, we discussed a fully discrete numerical scheme for the electrostatic Euler-Poisson equations with a given magnetic field. The scheme uses an operator split to treat the Euler subsystem and source subsystem separately. The Euler subsystem is treated explicitly with a graph viscosity method that is invariant domain preserving and conservative. The source subsystem, which couples the electrostatic potential, the momentum, and the magnetic field, exhibits multiscale phenomena that operate at various timescales spanning many orders of magnitude. To address this issue, while also maintaining an energy balance, we solved the source system implicitly with a PDE Schur complement that reduces to solving a Poisson type

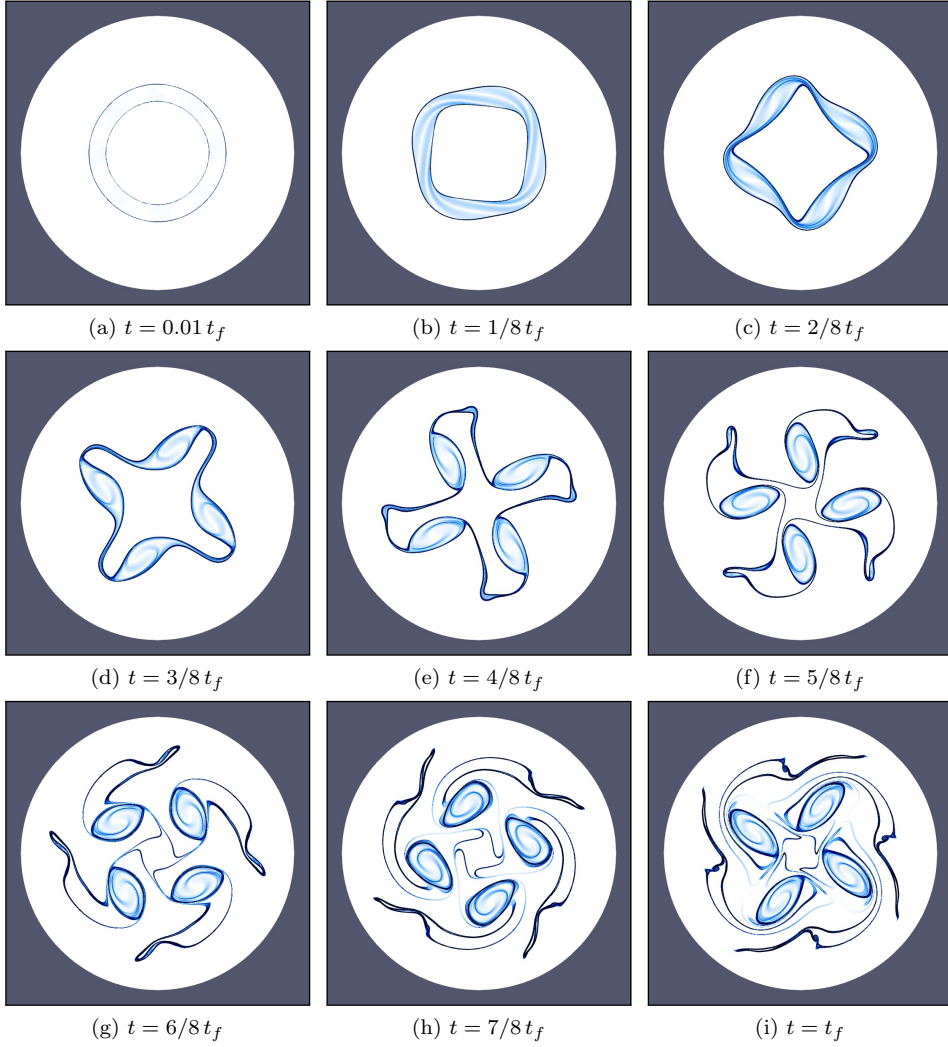


Fig. 5.2: Temporal snapshots of a schlieren plot of the density profile of the fourth mode diocotron instability test case. Reference computation with no restart on refinement level $r = 9$ amounting to 12,582,912 dG degrees of freedom per component. Here, $t_f = 10$.

problem at each time step. We proved that the full numerical scheme preserves the desired structure of the PDE system, and we demonstrated that the scheme performs well in the magnetic drift limit without having to resolve high-frequency oscillations. For future work, we will adapt the methods presented here to the full Euler-Maxwell system where both the electrostatic potential and the magnetic field are not given but instead computed self-consistently from Maxwell's equations.

Acknowledgments. JH and MM: acknowledge partial support by the National Science Foundation under grant DMS-2045636 and by the Air Force Office of Sci-

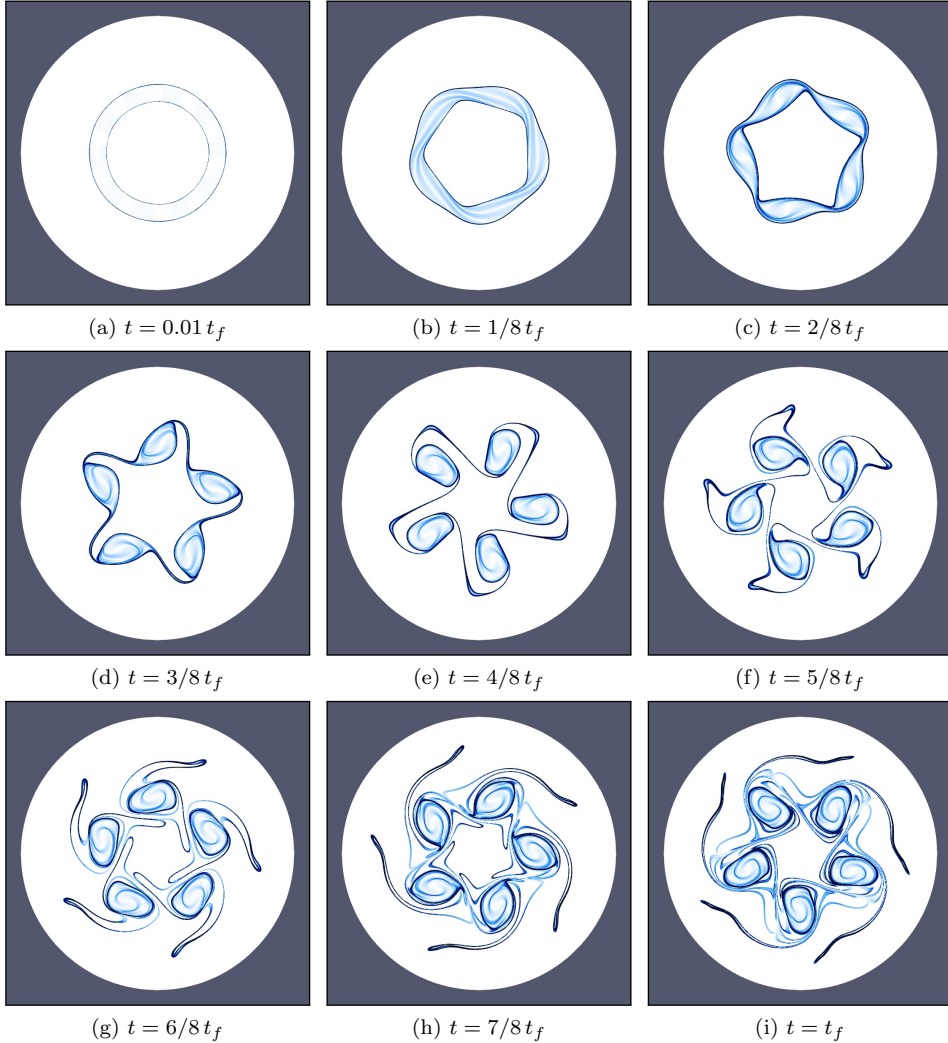
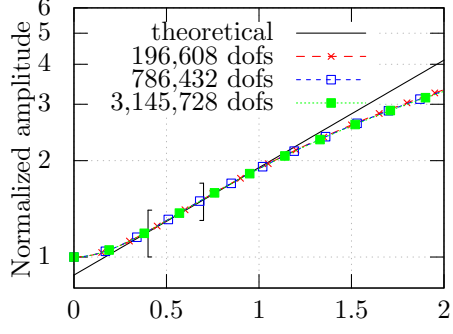
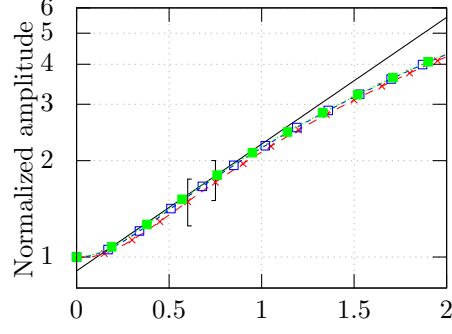
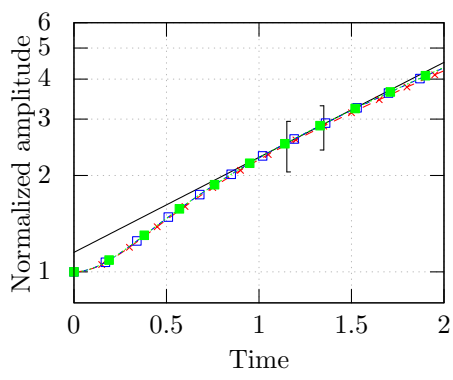


Fig. 5.3: Temporal snapshots of a schlieren plot of the density profile of the fifth mode diocotron instability test case. Reference computation with no restart on refinement level $r = 9$ amounting to 12,582,912 dG degrees of freedom per component. Here, $t_f = 10$.

tific Research, USAF, under grant/contract number FA9550-23-1-0007. IT: has been supported by the Department of Energy under grant/contract LDRD-CIS-226834, the National Science Foundation under grant DMS-2409841, and by a Simons Travel Award MPS-TSM-00007151. JNS: This work was partially supported by the Laboratory Directed Research and Development program at Sandia National Laboratories, and by U.S. Department of Energy, Office of Science (SC), Office of Advanced Scientific Computing Research's [Applied Mathematics / Computer Science / Advanced Computing Technologies] Competitive Portfolios program. Sandia is a multimission laboratory managed and operated by National Technology and Engineering Solutions

(a) $\ell = 3$ (b) $\ell = 4$ (c) $\ell = 5$

ℓ	dofs	$\gamma_{\ell,h}$	deviation
3	196,608	0.777	0.005
	786,432	0.775	0.003
	3,145,728	0.773	0.001
4	196,608	0.935	0.024
	786,432	0.919	0.008
	3,145,728	0.913	0.002
5	196,608	0.667	0.016
	786,432	0.677	0.006
	3,145,728	0.680	0.003

(d) Growth rates

Fig. 5.4: Theoretical versus computed growth rates for modes (a) 3, (b) 4, and (c) 5. Log scale on the y axis. Numerical growth rates are computed from the numerical amplitudes by fitting an exponential curve to the data between the square brackets in the plots from (a) $t = 0.4$ to $t = 0.7$, (b) $t = 0.6$ to $t = 0.75$, (c) $t = 1.15$ to $t = 1.35$. The numerical growth rates and their deviations from the theoretical growth rate (a) $\gamma_3 \approx 0.772$, (b) $\gamma_4 \approx 0.911$, (c) $\gamma_5 \approx 0.683$ are given in (d).

of Sandia LLC, a wholly owned subsidiary of Honeywell International Inc. for the U.S. Department of Energy's National Nuclear Security Administration under contract DE-NA0003525.

Appendix A. Barotropic closures. We consider the case of the compressible Euler equations with barotropic closure. In this case: the pressure is given by $p = p(\rho)$, the sound speed is $c = p'(\rho)$, and the specific internal energy is given by $e = e(\rho) = \int^\rho r^{-2} p(r) dr$, which leads to the following entropy-dissipation balance for the barotropic Euler system:

$$\frac{d}{dt} \int_D \frac{1}{2\rho} |\mathbf{m}|^2 + \rho e(\rho) dx + \int_0^t \left\{ \int_{\partial D} \left(\frac{1}{2\rho} |\mathbf{m}|^2 + \rho e(\rho) + p(\rho) \right) \mathbf{v} \cdot \mathbf{n} d\sigma_x \right\} dt \leq 0.$$

This motivates the following definitions:

$$(A.1) \quad \eta(\mathbf{u}) := \frac{1}{2\rho}|\mathbf{m}|^2 + \rho e(\rho) \quad \text{and} \quad \mathbf{q}(\mathbf{u}) := \left(\frac{1}{2\rho}|\mathbf{m}|^2 + \rho e(\rho) + p(\rho)\right)\mathbf{v},$$

for the mathematical entropy and entropy-flux, respectively. For the specific case of the isothermal closure $p(\rho) = \theta\rho$, the specific internal energy takes the form $e = e(\rho) = \theta \ln \rho$.

Appendix B. Hyperbolic solver. This section provides a brief outline of the numerical methods used to solve the compressible Euler subsystem for all the computational experiments advanced in Section 5. This section does not introduce any novel concept, idea, or numerical scheme, and it is only provided for the sake of completeness. The main ideas advanced in this section were originally developed in the sequence of papers [27, 28, 29, 30] and revised, for the case of discontinuous spatial discretizations, in [36]. In this brief appendix, we limit ourselves to describe the first-order scheme. For the implementation of higher order schemes we refer the reader to [36].

The low-order scheme is obtained by using a first-order graph viscosity method suggested first in [29] while also handling the boundary conditions as described in [36]. Let t_n be the current time, τ_n the current time step, and advance in time by setting $t_{n+1} = t_n + \tau_n$. Let $\mathbf{u}_h^n = \sum_{i \in \mathcal{V}} \mathbf{u}_i^n \phi_i(\mathbf{x})$ be the finite element approximation at time t_n . The first order approximation at time t_{n+1} is computed as

$$(B.1) \quad m_i \frac{\mathbf{u}_i^{L,n+1} - \mathbf{u}_i^n}{\tau_n} + \sum_{j \in \mathcal{I}(i)} \mathbf{f}(\mathbf{u}_j^n) \mathbf{c}_{ij} - d_{ij}^L (\mathbf{u}_j^n - \mathbf{u}_i^n) \\ + \mathbf{f}(\mathbf{u}_i^{\partial D,n}) \mathbf{c}_i^{\partial D} - d_i^L (\mathbf{u}_i^{\partial D,n} - \mathbf{u}_i^n) = \mathbf{0},$$

where m_i is the lumped mass entry corresponding to the shape function $\phi_i(\mathbf{x})$, the vectors $\mathbf{c}_{ij} \in \mathbb{R}^d$ and $\mathbf{c}_i^{\partial D} \in \mathbb{R}^d$ were defined in formulas (2.10)-(2.11) of reference [36]. The vector $\mathbf{c}_i^{\partial D}$ is zero, unless the corresponding collocation point \mathbf{x}_i lies on the boundary ∂D [36]. The set $\mathcal{I}(i)$ is the so-called stencil which is defined as $\mathcal{I}(i) = \{j \in \mathcal{V} \mid \mathbf{c}_{ij} \neq \mathbf{0}\}$, $\mathbf{f}(\mathbf{u}) \in \mathbb{R}^{(d+2) \times d}$ is the usual Euler flux $\mathbf{f}(\mathbf{u}) = [\mathbf{m}^\top, \rho^{-1} \mathbf{m} \mathbf{m}^\top + \mathbb{I} p, \rho^{-1} \mathbf{m}^\top (\mathcal{E} + p)]$. For the case of barotropic models $\mathbf{f}(\mathbf{u}) \in \mathbb{R}^{(d+1) \times d}$ is defined as $\mathbf{f}(\mathbf{u}) = [\mathbf{m}^\top, \rho^{-1} \mathbf{m} \mathbf{m}^\top + \mathbb{I} p]$. The state $\mathbf{u}_i^{\partial D,n}$ corresponds with boundary data which is assumed to be known. The low-order graph-viscosities $d_{ij}^{L,n} > 0$ and $d_i^{L,n} > 0$ in (B.1) are computed as:

$$(B.2) \quad \begin{cases} d_{ij}^{L,n} := |\mathbf{c}_{ij}|_{\ell^2} \lambda_{\max}(\mathbf{u}_i^n, \mathbf{u}_j^n, \mathbf{n}_{ij}), & \text{where } \mathbf{n}_{ij} = \frac{\mathbf{c}_{ij}}{|\mathbf{c}_{ij}|_{\ell^2}}, \quad \text{for } i \neq j, \\ d_i^{L,n} := |\mathbf{c}_i^{\partial D}|_{\ell^2} \lambda_{\max}(\mathbf{u}_i^n, \mathbf{u}_i^{\partial D,n}, \mathbf{n}_i), & \text{where } \mathbf{n}_i = \frac{\mathbf{c}_i^{\partial D}}{|\mathbf{c}_i^{\partial D}|_{\ell^2}}. \\ d_{ii}^{L,n} := - \sum_{j \in \mathcal{I}(i), j \neq i} d_{ij}^{L,n} - d_i^{L,n}. \end{cases}$$

Here $\lambda_{\max}(\mathbf{u}_L, \mathbf{u}_R, \mathbf{n})$ is the maximum wave speed of the one dimensional Riemann problem: $\partial_t \mathbf{u} + \partial_x (\mathbf{f}(\mathbf{u}) \mathbf{n}) = 0$, where $\mathbf{x} = \mathbf{x} \cdot \mathbf{n}$, with initial condition: $\mathbf{u}(x, 0) = \mathbf{u}_L = [\rho_L, \mathbf{m}_L, \mathcal{E}_L]^\top$ if $x < 0$, and $\mathbf{u}(x, 0) = \mathbf{u}_R = [\rho_R, \mathbf{m}_R, \mathcal{E}_R]^\top$ if $x \geq 0$. The maximum wavespeed of this Riemann problem can be computed exactly [49, Chap. 4] for the co-volume equations of state, however this comes at the expense of solving a nonlinear

problem. In theory and practice, any upper bound of the maximum wavespeed of the Riemann problem could be used in formula (B.2) while still preserving rigorous mathematical properties of the scheme [29, 30]. We will denote, generically, any estimate of the maximum wavespeed as $\lambda^\#(\mathbf{u}_L, \mathbf{u}_R, \mathbf{n})$. For all the computations reported in this paper we use the following maximum wavespeed estimates.

For the case of the co-volume equation of state, the pressure is given by $p(1-b\rho) = (\gamma-1)e\rho$ with $b \geq 0$. In this case, we use $\lambda^\#(\mathbf{u}_L, \mathbf{u}_R, \mathbf{n})$ defined by:

$$\begin{aligned}
 (B.3) \quad \lambda^\#(\mathbf{u}_L, \mathbf{u}_R, \mathbf{n}) &= \max((\lambda_1^-(p^\#))_-, (\lambda_3^+(p^\#))_+), \\
 \lambda_1^-(p^\#) &= v_L - c_L \left(1 + \frac{\gamma+1}{2\gamma} \left(\frac{p^\# - p_L}{p_L} \right)_+ \right)^{\frac{1}{2}}, \\
 \lambda_3^+(p^\#) &= v_R + c_R \left(1 + \frac{\gamma+1}{2\gamma} \left(\frac{p^\# - p_R}{p_R} \right)_+ \right)^{\frac{1}{2}}, \\
 (B.4) \quad p^\# &:= \left(\frac{c_L(1-b\rho_L) + c_R(1-b\rho_R) - \frac{\gamma-1}{2}(v_R - v_L)}{c_L(1-b\rho_L) p_L^{\frac{\gamma-1}{2\gamma}} + c_R(1-b\rho_R) p_R^{\frac{\gamma-1}{2\gamma}}} \right)^{\frac{2\gamma}{\gamma-1}},
 \end{aligned}$$

where $z_- := \max(0, -z)$, $z_+ := \max(0, z)$, $v_L = \mathbf{v}_L \cdot \mathbf{n}$, $v_R = \mathbf{v}_R \cdot \mathbf{n}$, p_L and p_R are the left and right pressures, and c_L and c_R are left and right sound speeds. Formula (B.4) is often referred to as the two-rarefaction estimate [49]. It is possible to show that $\lambda^\#(\mathbf{u}_L, \mathbf{u}_R, \mathbf{n}) \geq \lambda_{\max}(\mathbf{u}_L, \mathbf{u}_R, \mathbf{n})$ for $1 < \gamma \leq \frac{5}{3}$, see [28]. We finally mention that scheme (B.1) equipped with the viscosity (B.3) guarantees the entropy-dissipation assumption (4.4).

If the pressure is independent of the specific internal energy, that is $p = p(\rho)$, and $p'(\rho) \geq 0$, we have that admissibility of the scheme only requires positivity of the density. In this context, the sound speed is simply given by $c = \sqrt{p'(\rho)}$. It can be proven that any choice of $\lambda^\#(\mathbf{u}_L, \mathbf{u}_R, \mathbf{n})$ satisfying the property $\lambda^\#(\mathbf{u}_L, \mathbf{u}_R, \mathbf{n}) \geq \max\{|\mathbf{v}_L \cdot \mathbf{n}|, |\mathbf{v}_R \cdot \mathbf{n}|\}$ is enough to guarantee positivity of the density. However, this is, in practice, not enough to tame the behaviour of non-smooth solutions. Therefore, for the case of a barotropic equation of state, we use

$$\lambda^\#(\mathbf{u}_L, \mathbf{u}_R, \mathbf{n}) = \max\{|\mathbf{v}_L \cdot \mathbf{n}|, |\mathbf{v}_R \cdot \mathbf{n}|\} + \max\{c_L, c_R\},$$

where $c_L = \sqrt{p'(\rho_L)}$ and $c_R = \sqrt{p'(\rho_R)}$. Note that this estimate of the maximum wavespeed is more than enough to guarantee admissibility of the solution. However, we make no claim as to whether this estimate is a sharp upper bound of the maximum wavespeed.

Remark B.1 (Convex reformulation and CFL condition). The scheme (B.1) can be rewritten as

$$(B.5) \quad \mathbf{u}_i^{\text{L},n+1} = \left(1 + \frac{2\tau_n d_{ii}^{\text{L},n}}{m_i} \right) \mathbf{u}_i^n + \frac{2\tau_n d_i^{\text{L},n}}{m_i} \bar{\mathbf{u}}_i^{\partial D,n} + \sum_{j \in \mathcal{I}(i) \setminus \{i\}} \frac{2\tau_n d_{ij}^{\text{L},n}}{m_i} \bar{\mathbf{u}}_{ij}^n,$$

where $\bar{\mathbf{u}}_{ij}^n$ and $\bar{\mathbf{u}}_i^{\partial D, n}$ are the bar-states defined by

$$(B.6) \quad \bar{\mathbf{u}}_{ij}^n = \frac{1}{2}(\mathbf{u}_j^n + \mathbf{u}_i^n) - \frac{|\mathbf{c}_{ij}|}{2d_{ij}^L} (\mathbb{f}(\mathbf{u}_j^n) - \mathbb{f}(\mathbf{u}_i^n)) \mathbf{n}_{ij},$$

$$(B.7) \quad \bar{\mathbf{u}}_i^{\partial D, n} = \frac{1}{2}(\mathbf{u}_i^{\partial D, n} + \mathbf{u}_i^n) - \frac{|\mathbf{c}_i^{\partial D}|}{2d_i^L} (\mathbb{f}(\mathbf{u}_i^{\partial D, n}) - \mathbb{f}(\mathbf{u}_i^n)) \mathbf{n}_i.$$

We note that the states $\{\bar{\mathbf{u}}_{ij}^n\}_{j \in \mathcal{I}(i)}$ are admissible, provided that \mathbf{u}_i^n and \mathbf{u}_j^n are admissible [29, 30, 36]. We also note that \mathbf{u}_i^{n+1} is a convex combination of the bar-states $\{\bar{\mathbf{u}}_{ij}^n\}_{j \in \mathcal{I}(i)}$ and $\bar{\mathbf{u}}_i^{\partial D, n}$ provided the condition $(1 + \frac{2\tau_n d_{ii}^L}{m_i}) \geq 0$ holds. Therefore, we define the largest admissible time-step size as

$$(B.8) \quad \tau_n = \text{CFL} \cdot \min_{i \in \mathcal{V}} \left(-\frac{m_i}{2d_{ii}^L} \right)$$

where $\text{CFL} \in (0, 1)$ is a user defined parameter.

Describing the extension of this scheme to higher order accuracy is beyond the scope of this paper. Here, we briefly mention that the second-order accurate scheme used for all our computations uses (exactly) the flux-limited high-order method described in [36]. For the case of the barotropic Euler system, we implemented the entropy-viscosity method as described in [36] using the entropy-flux pair defined in (A.1).

References.

- [1] P. C. AFRICA, D. ARNDT, W. BANGERTH, B. BLAIS, M. FEHLING, R. GASSMÖLLER, T. HEISTER, L. HELTAI, S. KINNEWIG, M. KRONBICHLER, M. MAIER, P. MUNCH, M. SCHRETER-FLEISCHHACKER, J. P. THIELE, B. TURCKSIN, D. WELLS, AND V. YUSHUTIN, *The deal.II Library, Version 9.6*, Journal of Numerical Mathematics, 32 (2024), pp. 369–380.
- [2] D. ARNDT, W. BANGERTH, D. DAVYDOV, T. HEISTER, L. HELTAI, M. KRONBICHLER, M. MAIER, J.-P. PELTERET, B. TURCKSIN, AND D. WELLS, *The deal.II finite element library: design, features, and insights*, Computers & Mathematics with Applications, 81 (2021), pp. 407–422.
- [3] N. BEN ABDALLAH AND R. EL HAJJ, *Diffusion and guiding center approximation for particle transport in strong magnetic fields*, Kinet. Relat. Models, 1 (2008), pp. 331–354.
- [4] J. A. BITTENCOURT, *Fundamentals of plasma physics*, Springer Science & Business Media, 2004.
- [5] M. BOSTAN, *The Vlasov-Maxwell system with strong initial magnetic field: guiding-center approximation*, Multiscale Model. Simul., 6 (2007), pp. 1026–1058.
- [6] S. BRULL, P. DEGOND, F. DELUZET, AND A. MOUTON, *Asymptotic-preserving scheme for a bi-fluid Euler-Lorentz model*, Kinet. Relat. Models, 4 (2011), pp. 991–1023.
- [7] F. F. CHEN ET AL., *Introduction to plasma physics and controlled fusion*, vol. 1, Springer, 1984.
- [8] T. C. CLEVENGER, T. HEISTER, G. KANSCHAT, AND M. KRONBICHLER, *A flexible, parallel, adaptive geometric multigrid method for FEM*, ACM Trans. Math. Softw., 47 (2021), pp. 7/1–27.
- [9] M. CROCKATT AND J. SHADID, *Development, Implementation, and Verification of Partially-Ionized Collisional Multifluid Plasma Models in Drekar*, Tech. Report

SAND2021-7427, 1817837, 698871, Sandia National Laboratories, Albuquerque, NM, June 2021.

- [10] M. M. CROCKATT, S. MABUZA, J. N. SHADID, S. CONDE, T. M. SMITH, AND R. P. PAWLOWSKI, *An implicit monolithic afe stabilization method for the cg finite element discretization of the fully-ionized ideal multifluid electromagnetic plasma system*, Journal of Computational Physics, 464 (2022), p. 111228.
- [11] M. M. CROCKATT AND J. N. SHADID, *A non-neutral generalized ohm's law model for magnetohydrodynamics in the two-fluid regime*, Physics of Plasmas, 30 (2023), p. 053902.
- [12] T. A. DAO, M. NAZAROV, AND I. TOMAS, *A structure preserving numerical method for the ideal compressible MHD system*, J. Comput. Phys., 508 (2024), pp. Paper No. 113009, 25.
- [13] R. C. DAVIDSON AND G. M. FELICE, *Influence of profile shape on the diocotron instability in a non-neutral plasma column*, Physics of Plasmas, 5 (1998), pp. 3497–3511. Publisher: AIP Publishing.
- [14] P. DEGOND, F. DELUZET, A. SANGAM, AND M.-H. VIGNAL, *An asymptotic preserving scheme for the Euler equations in a strong magnetic field*, J. Comput. Phys., 228 (2009), pp. 3540–3558.
- [15] F. DELUZET, M. OTTAVIANI, AND S. POSSANNER, *A drift-asymptotic scheme for a fluid description of plasmas in strong magnetic fields*, Comput. Phys. Commun., 219 (2017), pp. 164–177.
- [16] A. ERN AND J.-L. GUERMOND, *Invariant-domain-preserving high-order time stepping: I. explicit runge–kutta schemes*, SIAM Journal on Scientific Computing, 44 (2022), pp. A3366–A3392.
- [17] A. ERN AND J.-L. GUERMOND, *Invariant-domain preserving high-order time stepping: II. imex schemes*, SIAM Journal on Scientific Computing, 45 (2023), pp. A2511–A2538.
- [18] E. FEIREISL, *Dynamics of viscous compressible fluids*, vol. 26 of Oxford Lecture Series in Mathematics and its Applications, Oxford University Press, Oxford, 2004.
- [19] F. FILBET AND L. M. RODRIGUES, *Asymptotically stable particle-in-cell methods for the Vlasov-Poisson system with a strong external magnetic field*, SIAM J. Numer. Anal., 54 (2016), pp. 1120–1146.
- [20] E. FRÉNOD, S. A. HIRSTOAGA, M. LUTZ, AND E. SONNENDRÜCKER, *Long time behaviour of an exponential integrator for a Vlasov-Poisson system with strong magnetic field*, Commun. Comput. Phys., 18 (2015), pp. 263–296.
- [21] E. FRÉNOD AND E. SONNENDRÜCKER, *Homogenization of the Vlasov equation and of the Vlasov-Poisson system with a strong external magnetic field*, Asymptot. Anal., 18 (1998), pp. 193–213.
- [22] E. FRÉNOD AND E. SONNENDRÜCKER, *Long time behavior of the two-dimensional Vlasov equation with a strong external magnetic field*, Math. Models Methods Appl. Sci., 10 (2000), pp. 539–553.
- [23] J. H. GOEDBLOED, J. GOEDBLOED, AND S. POEDTS, *Principles of magnetohydrodynamics: with applications to laboratory and astrophysical plasmas*, Cambridge university press, 2004.
- [24] F. GOLSE AND L. SAINT-RAYMOND, *The Vlasov-Poisson system with strong magnetic field*, J. Math. Pures Appl. (9), 78 (1999), pp. 791–817.
- [25] J.-L. GUERMOND, M. KRONBICHLER, M. MAIER, B. POPOV, AND I. TOMAS, *On the implementation of a robust and efficient finite element-based parallel solver for the compressible Navier-Stokes equations*, Computer Methods in Ap-

plied Mechanics and Engineering, 389 (2022), p. 114250.

[26] J.-L. GUERMOND, M. MAIER, B. POPOV, AND I. TOMAS, *Second-order invariant domain preserving approximation of the compressible Navier-Stokes equations*, Comput. Methods Appl. Mech. Engrg., 375 (2021), pp. Paper No. 113608, 17.

[27] J.-L. GUERMOND, M. NAZAROV, B. POPOV, AND I. TOMAS, *Second-order invariant domain preserving approximation of the Euler equations using convex limiting*, SIAM J. Sci. Comput., 40 (2018), pp. A3211–A3239.

[28] J.-L. GUERMOND AND B. POPOV, *Fast estimation from above of the maximum wave speed in the Riemann problem for the Euler equations*, J. Comput. Phys., 321 (2016), pp. 908–926.

[29] J.-L. GUERMOND AND B. POPOV, *Invariant domains and first-order continuous finite element approximation for hyperbolic systems*, SIAM J. Numer. Anal., 54 (2016), pp. 2466–2489.

[30] J.-L. GUERMOND, B. POPOV, AND I. TOMAS, *Invariant domain preserving discretization-independent schemes and convex limiting for hyperbolic systems*, Comput. Methods Appl. Mech. Engrg., 347 (2019), pp. 143–175.

[31] A. HAMIAZ, M. MEHRENBERGER, A. BACK, AND P. NAVARO, *Guiding center simulations on curvilinear grids*, in CEMRACS 2014—numerical modeling of plasmas, vol. 53 of ESAIM Proc. Surveys, EDP Sci., Les Ulis, 2016, pp. 99–119.

[32] D. HAN-KWAN, *Effect of the polarization drift in a strongly magnetized plasma*, ESAIM Math. Model. Numer. Anal., 46 (2012), pp. 929–947.

[33] M. HERDA, *On massless electron limit for a multispecies kinetic system with external magnetic field*, J. Differential Equations, 260 (2016), pp. 7861–7891.

[34] M. KRONBICHLER AND K. KORMANN, *A generic interface for parallel cell-based finite element operator application*, Comput. Fluids, 63 (2012), pp. 135–147.

[35] M. KRONBICHLER AND K. KORMANN, *Fast matrix-free evaluation of discontinuous Galerkin finite element operators*, ACM Trans. Math. Softw., 45 (2019), pp. 29/1–40.

[36] M. KRONBICHLER, M. MAIER, AND I. TOMAS, *Graph-based methods for hyperbolic systems of conservation laws using discontinuous space discretizations*, Communications in Computational Physics, 38 (2025), pp. 74–108.

[37] M. KRONBICHLER AND W. A. WALL, *A performance comparison of continuous and discontinuous Galerkin methods with fast multigrid solvers*, SIAM J. Sci. Comput., 40 (2018), pp. A3423–A3448.

[38] A. LA SPINA AND J. FISH, *A hybridizable discontinuous Galerkin formulation for the Euler–Maxwell plasma model*, Journal of Computational Physics, 496 (2024).

[39] M. MAIER AND M. KRONBICHLER, *Efficient parallel 3d computation of the compressible euler equations with an invariant-domain preserving second-order finite-element scheme*, ACM Transactions on Parallel Computing, 8 (2021), pp. 16:1–30.

[40] M. MAIER, J. SHADID, AND I. TOMAS, *Structure-preserving finite-element schemes for the Euler–Poisson equations*, Communications in Computational Physics, 33 (2023), pp. 647–691.

[41] F. MOTTEZ, *A guiding centre direct implicit scheme for magnetized plasma simulations*, J. Comput. Phys., 227 (2008), pp. 3260–3281.

[42] J. PÉTRI, *The diocotron instability in a pulsar cylindrical electroosphere*, Astronomy and Astrophysics, 464 (2006).

[43] J. PÉTRI, *Non-linear evolution of the diocotron instability in a pulsar electroosphere: two-dimensional particle-in-cell simulations*, Astronomy & Astrophysics,

503 (2009), pp. 1–12.

[44] J. PÉTRI, J. HEYVAERTS, AND S. BONAZZOLA, *Diocotron instability in pulsar electroospheres-i. linear analysis*, *Astronomy & Astrophysics*, 387 (2002), pp. 520–530.

[45] X. PIAO, P. KIM, AND D. KIM, *One-step $L(\alpha)$ -stable temporal integration for the backward semi-Lagrangian scheme and its application in guiding center problems*, *J. Comput. Phys.*, 366 (2018), pp. 327–340.

[46] A. QUARTERONI AND A. VALLI, *Numerical approximation of partial differential equations*, vol. 23 of Springer Series in Computational Mathematics, Springer-Verlag, Berlin, 1994.

[47] I. TOMAS, J. SHADID, M. CROCKATT, R. PAWLOWSKI, M. MAIER, AND J.-L. GUERMOND, *Final report of activities for the LDRD-express project 223796 titled: Fluid models of charged species transport: numerical methods with mathematically guaranteed properties*, tech. report, Sandia National Laboratories, Albuquerque, NM, 2021.

[48] I. TOMAS, J. SHADID, M. MAIER, AND A. SALGADO, *Final report of activities for the LDRD-CIS project 226834 titled: Asymptotic preserving methods for fluid electron-fluid models in the large magnetic field limit with mathematically guaranteed properties*, tech. report, Sandia National Laboratories, Albuquerque, NM, 2022.

[49] E. F. TORO, *Riemann solvers and numerical methods for fluid dynamics*, Springer-Verlag, Berlin, third ed., 2009. A practical introduction.

[50] Y. A. TSIDULKO, *Two-dimensional dynamics of two-component plasma with finite β* , *Phys. Plasmas*, 11 (2004), pp. 4420–4428.